

# A Search for Electron Neutrino Transitions to Sterile States in the BEST Experiment

V.V. Barinov, S.N. Danshin, V.N. Gavrin,\* V.V. Gorbachev, D.S. Gorbunov,  
T.V. Ibragimova, Yu.P. Kozlova, L.V. Kravchuk, V.V. Kuzminov, B.K. Lubsandorzhev,  
Yu.M. Malyshkin, I.N. Mirmov, A.A. Shikhin, and E.P. Veretenkin  
*Institute for Nuclear Research of the Russian Academy of Sciences, Moscow 117312, Russia*

B.T. Cleveland  
*SNOLAB, Sudbury, ON P3Y 1N2, Canada*

H. Ejiri  
*Research Center for Nuclear Physics, Osaka University, Osaka, Japan*

S.R. Elliott, I. Kim, and R. Massarczyk  
*Los Alamos National Laboratory, Los Alamos, NM, USA*

D. Frekers  
*Institut für Kernphysik, Westfälische Wilhelms-Universität Münster, D-48149 Münster, Germany*

W.C. Haxton  
*Nuclear Science Division, Lawrence Berkeley National Laboratory, Berkeley, CA 94720, USA and  
Department of Physics, University of California, Berkeley, CA 94720, USA*

V.A. Matveev and G.V. Trubnikov  
*Joint Institute for Nuclear Research (JINR) Joliot-Curie 6, 141980, Dubna, Moscow Region, Russia*

J.S. Nico  
*National Institute of Standards and Technology, 100 Bureau Dr, Gaithersburg, MD 20899, USA*

A.L. Petelin, V.A. Tarasov, and A.I. Zvir  
*JSC 'State Scientific Center Research Institute of Atomic Reactors', Dimitrovgrad, 433510, Russia*

R.G.H. Robertson  
*Center for Experimental Nuclear Physics and Astrophysics, and Department  
of Physics, University of Washington, Seattle, WA 98195, USA*

D. Sinclair  
*Carleton University 1125 Colonel By Drive Ottawa, K1S 5B6, Canada*

J.F. Wilkerson  
*Department of Physics and Astronomy, University of North Carolina, Chapel Hill, NC 27599, USA and  
Triangle Universities Nuclear Laboratory, Durham, NC 27708, USA*

(Dated: May 10, 2022)

The Baksan Experiment on Sterile Transitions (BEST) probes the gallium anomaly and its possible connections to oscillations between active and sterile neutrinos. Based on the Gallium-Germanium Neutrino Telescope (GGNT) technology of the SAGE experiment, BEST employs two zones of liquid Ga target to explore neutrino oscillations on the meter scale. Oscillations on this short scale could produce deficits in the  $^{71}\text{Ge}$  production rates within the two zones, as well as a possible rate difference between the zones.

From July 5th to October 13th 2019, the two-zone target was exposed to a primarily monoenergetic, 3.4-MCi  $^{51}\text{Cr}$  neutrino source 10 times for a total of 20 independent  $^{71}\text{Ge}$  extractions from the two Ga targets. The  $^{71}\text{Ge}$  production rates from the neutrino source were measured from July 2019 to March 2020. At the end of these measurements, the counters were filled with  $^{71}\text{Ge}$  doped gas and calibrated during November 2020. In this paper, results from the BEST sterile neutrino oscillation experiment are presented in details. The ratio of the measured  $^{71}\text{Ge}$  production rates to the predicted rates for the inner and the outer target volumes are calculated from the known neutrino capture cross section. Comparable deficits in the measured ratios relative to predicted values are found for both zones, with the  $4\sigma$  deviations from unity consistent with the previously reported gallium anomaly. If interpreted in the context of neutrino oscillations, the deficits give best

fit oscillation parameters of  $\Delta m^2 = 3.3_{-2.3}^{+\infty} \text{ eV}^2$  and  $\sin^2 2\theta = 0.42_{-0.17}^{+0.15}$ , consistent with  $\nu_e \rightarrow \nu_s$  oscillations governed by a surprisingly large mixing angle.

## I. INTRODUCTION

Sterile neutrinos ( $\nu_s$ ) are hypothetical fermions which are singlets with respect to the Standard Model (SM) gauge groups [1–7]. Lacking electric, color, or hypercharges, they would not participate in electromagnetic, strong or weak interactions, but could through their gravitational interactions have consequences for astrophysics. In particular, sterile neutrinos could play a role in the formation of large-scale structure while evading the strong three-flavor constraints imposed from multiple experiments [8–14]. Sterile neutrinos naturally arise in many extensions of the Standard Model and have been invoked to account for various anomalies, including (for specific parameters) dark matter.

The existence of singlet state neutrinos is theoretically well-motivated. Neutrinos are the only fermions known to have an intrinsic left-handed chirality. When their right-handed counterparts are considered, the simplest neutrino mass generation model of the type-I seesaw mechanism is allowed [15–18]. The inactive right-handed neutrinos have so-called Majorana masses independent of the Higgs mechanism and can generate neutrino masses at any scale. Assuming the existence of sterile neutrinos can therefore not only explain the non-zero mass of neutrinos but also account for neutrino masses being at least 5 orders of magnitude smaller than the electron rest mass.

All plausible couplings of sterile neutrinos are weak and are thought to be beyond the detection capability of the current detectors. Hence, the only possibility for detecting sterile neutrinos is to observe the mixing with active neutrinos. In general, extensions of the SM to include sterile neutrinos do not impose strong constraints on their masses. While sterile neutrinos have been proposed with masses ranging from sub-eV to GUT scales, the 1 eV scale is particularly interesting as multiple physical phenomena can be explained by a single hypothesis. Such indications include unexplained excesses in the electron neutrino fluxes in LSND [19, 20] and MiniBooNE experiments; reactor antineutrino anomalies at 10-100 m oscillation lengths [21–23]; and the anomalous deficits in the radiochemical-source measurements of the SAGE [24, 25] and the GALLEX [26, 27] experiments. Recent results from MicroBooNE indicate a discrepancy with the MiniBooNE result [28], but do not rule out the sterile neutrino hypothesis [29, 30].

The Baksan Experiment on Sterile Transitions (BEST) is a two-distance oscillation experiment designed to explore the deficit of electron neutrinos ( $\nu_e$ ) previously reported in the SAGE and GALLEX source experiments,

commonly known as the gallium anomaly. The experimental design is presented in Fig. 1, with the flowchart showing the experimental steps in Fig. 2. About 47 tonnes of liquid Ga metal, divided into two concentric zones, serve as the target for the charged-current reaction  ${}^{71}\text{Ga}(\nu_e, e) {}^{71}\text{Ge}$ . The decay of the mainly monoenergetic neutrino source of the  ${}^{51}\text{Cr}$  isotope is via electron capture with the emission of  $\nu_e$  in four spectral lines. The  $\nu_e$  energies and their branching ratios are: 747 keV (81.63%), 427 keV (8.95%), 752 keV (8.49%) and 432 keV (0.93%) [31]. The source was placed at the center of the two zones of the Ga target, irradiating the two volumes simultaneously. This allows the production rates of  ${}^{71}\text{Ge}$  to be measured at two different distances. As the sizes of the two target zones are roughly at a meter scale, BEST has a high sensitivity to the oscillatory behaviour in the  $\nu_e$  flux at the same scale, which corresponds to  $\Delta m^2 \approx 1 \text{ eV}^2$ . Neutrino oscillations at this short scale would be indicated by deficits in the  ${}^{71}\text{Ge}$  production rates within the two zones, as well as the differences between them. The use of an electron capture  $\nu_e$  source is a powerful technique to search for neutrino oscillations. The  $\nu_e$  spectrum is simple, being comprised of a dominant monoenergetic component and 3 sub-dominant lines. It is a well-understood spectrum relying on well-known nuclear and atomic physics parameters.

In this article, we present the results from the BEST  $\nu_s$  oscillation search experiment. Section II describes the geometry of the two-zone gallium target which is irradiated by a  ${}^{51}\text{Cr}$   $\nu_e$  source. Section III reviews how the  ${}^{71}\text{Ge}$  atoms are extracted from the target volumes and transferred to the proportional counters. Section IV is devoted to a description of the counter systems which measure the  ${}^{71}\text{Ge}$  decay rates. In Section V, techniques of candidate event selection and analysis to set the exclusion within the  $(\Delta m^2, \sin^2(2\theta))$  oscillation parameter space are introduced. We discuss the first result from the BEST experiment in Section VI, and conclude in Section VII that our result is consistent with the neutrino oscillation hypothesis with  $\Delta m^2 > 1 \text{ eV}^2$  sterile neutrinos.

## II. TARGET GEOMETRY

The Baksan Neutrino Observatory (BNO) is located in a dedicated underground laboratory in the northern Caucasus mountains of Russia. Located 3.5 km below the surface, the deep underground laboratory has an overburden of 4700 meters-water-equivalent (mwe), resulting in muon flux in the laboratory of  $(3.03 \pm 0.10) \times 10^{-9} / (\text{cm}^2 \text{ s})$  [25]. The entirety of the laboratory is lined with 60 cm of radiopure concrete and 6 mm steel shell to reduce  $\gamma$  and neutron backgrounds from rocks.

The concentric two-zone gallium target of the BEST

---

\* gavrin@inr.ru

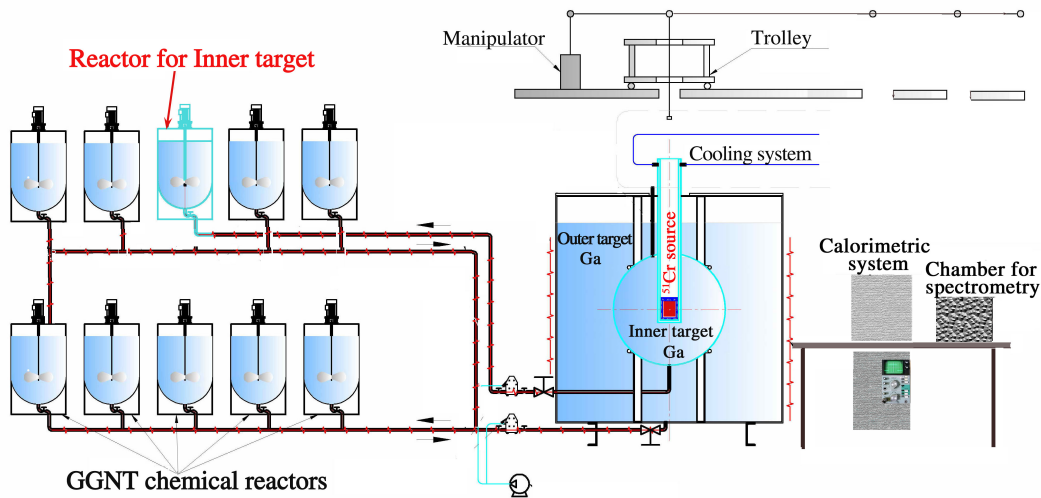


FIG. 1. The Ga target and extraction piping diagram also indicating the source handling apparatus.

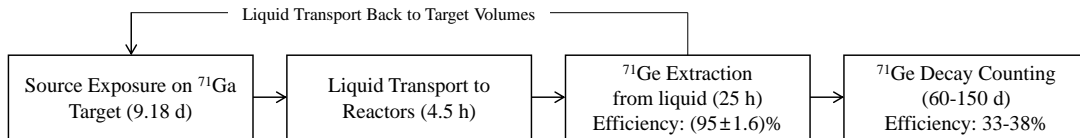


FIG. 2. Flowchart showing the experimental steps of the BEST experiment. Time spent on each step and relevant efficiencies are also presented.

experiment is located in the main hall of the laboratory. The inner spherical volume with inner diameter 133.5 cm contains  $(7.4691 \pm 0.0631)$  t of liquid Ga, and the outer cylindrical volume with inner diameter 218 cm and maximum Ga target height 211.2 cm contains  $(39.9593 \pm 0.0024)$  t of Ga. The Ga metal, heated to  $30.0$  °C, remains molten inside the volumes. The carrier Ge and any produced  $^{71}\text{Ge}$  was extracted at the end of each exposure for the calculation of production rates. The extraction procedures are explained in Sec. V G 1, and discussed more thoroughly in Ref. [32].

The  $^{51}\text{Cr}$  source with known activity was contained in a cylindrical cartridge with a radius of 4.3 cm and height of 10.8 cm. This source assembly was placed in a specially constructed tungsten radiation shield with a thickness of  $\approx 30$  mm and a weight of 42.8 kg, which provides radiation safety from gamma activity from the source, and a steel shell with a special cap for capturing the source by a manipulator. The assembly was placed at the center of the two zones to irradiate both volumes simultaneously.

The source was delivered to BNO on July 5, 2019 and was placed into the two-zone target at 14:02 local time (UTC+3) that same day, and this is our chosen reference time for the source strength. The source was manufactured by irradiating 4 kg of  $^{50}\text{Cr}$ -enriched metal for 100 d in a reactor at the State Scientific Center Research Institute of Atomic Reactors, Dimitrovgrad,

Russia. The activity ( $A$ ) of the source is measured by calorimetric method based on the heat released by the source [33, 34]. At the end of each extraction, the source is moved into a lead container for the activity measurement. The  $\gamma$  spectrum is measured at 21.65 m distance with a Ge detector for an hour. After the spectral measurement, the source is moved to the calorimeter to measure the heat emitted by the source for 20-21 hours. The tungsten shield of the source does not affect calorimetry as the shield is included within the calorimeter. Moreover, it helps by absorbing gamma radiation from impurities in the source, increasing the accuracy of determining the heat release from  $^{51}\text{Cr}$ . Ten calorimetric measurements were performed after nine days of irradiation of gallium targets. The decay of  $^{51}\text{Cr}$  ( $\approx 90\%$  to the ground state and  $\approx 10\%$  to the excited state) releases on average  $(36.750 \pm 0.084)$  keV per decay event. From spectrometric measurements of gamma radiation of the source, the heat contribution from radioactive impurities is found to be  $(3.7 \pm 0.5)$  mW, which is  $5 \times 10^{-6}$  of the initial  $^{51}\text{Cr}$  source power. The measured activity of the source at the reference time is  $(3.414 \pm 0.008)$  MCi. The measured half-life of the  $^{51}\text{Cr}$  source is  $(27.710 \pm 0.017)$  days, which is in a good agreement with the known  $^{51}\text{Cr}$  half-life of  $(27.704 \pm 0.017)$  days [35]. A full description of the source and the calorimetric measurements of its intensity can be found in Refs. [33, 34].

### III. $^{71}\text{Ge}$ EXTRACTION

Between July 5th and October 13th 2019, the two-zone target was exposed to the source 10 times with an average exposure time of 9.18 d. The irradiation schedule was devised to maximize the number of extracted  $^{71}\text{Ge}$  atoms. The extraction was carried out at the end of each exposure. The first extraction counting periods were shorter in time due to the limited number of available counters. The shorter counting time has almost no effect on the number of calculated  $^{71}\text{Ge}$  decays but increases the statistical uncertainty due to the lower statistics of the measured counter background. After each exposure period, the Ga targets were transferred to chemical reactor vessels, and the produced  $^{71}\text{Ge}$  atoms were extracted from Ga with the technique almost identical to the one used for the SAGE experiment [25, 32]. Here we provide an overview.

The Ge carrier and the  $^{71}\text{Ge}$  atoms produced by the neutrino capture reaction are extracted from the Ga targets into an aqueous solution by adding a weak acidic solution of  $\text{H}_2\text{O}_2$  [36, 37], ensuring independent extractions of  $^{71}\text{Ge}$  atoms from each zone of the Ga target. The acid oxidizes the Ge metal and  $\text{GeH}_4$  is synthesized in gaseous form. Gallium is pumped out of the vessels until the aqueous acidic solution on the surface of gallium begins to be pumped out. The  $\text{GeH}_4$  is then mixed with Xe gas and introduced into a low-background proportional counter.

The extraction efficiency of Ge from a large mass of Ga is determined with high accuracy using mass spectrometry [38]. For BEST, the process of the efficiency estimation follows the same procedure as was used in SAGE. A known amount of stable  $^{72}\text{Ge}$  ( $2.4\ \mu\text{mol}$ , 92%) and  $^{76}\text{Ge}$  ( $2.4\ \mu\text{mol}$ , 95%) carriers were added to the volume in form of Ga-Ge alloy as the stable Ge carrier, and the molten Ga was stirred thoroughly to disperse the Ge throughout the volumes [32]. The total extraction efficiency is given by the ratio of the amount of Ge in the synthesized  $\text{GeH}_4$  to the initial amount of Ge in the Ga targets at the beginning of the exposure. Taking into account all the factors that can affect the extraction efficiency including the temperature, the amount of oxidizing agent ( $\text{H}_2\text{O}_2$ ), and the volume of the aqueous phase which defines the time of later concentration of Ge, the extraction procedure reached  $(98 \pm 0.2)\%$  efficiency from Ga, and the total efficiency including synthesis reached  $(95 \pm 1.6)\%$ . The extraction and exposure details for the inner and outer targets are summarized in Tables I and II, respectively. Due to the inefficiency of the extraction, a small proportion of the carrier Ge is still present within the Ga. The numbers of these carryover atoms were estimated and accounted for in the production rate calculation.

At each source exposure, gallium was pumped with the same levels into the two volumes, which were monitored by level sensors in the zones. Therefore, a larger mass of gallium was irradiated in solar neutrino exposures than

in exposures with a source. This contribution was also accounted for.

### IV. COUNTING OF $^{71}\text{Ge}$

The decay process  $^{71}\text{Ge} + e^- \rightarrow ^{71}\text{Ga} + \nu$  has a half-life of 11.4 d [39]. Two peaks at 10.4 keV (K peak) and 1.2 keV (L peak) are observable in the proportional counters. The K-capture, which constitutes  $\approx 88\%$  of all decays, can release 10.4 keV Auger electrons (41.5%), 1.2 keV Auger electrons with 9.2 keV X rays (41.2%), or 0.1 keV Auger electrons with 10.3 keV X rays (5.3%) [32]. On the other hand, L and M captures give almost entirely Auger electrons of energies 1.2 keV and 0.12 keV respectively [32]. Since the proportional counters have much higher efficiency for Auger electrons than for the X rays, the number of K and L peak counts are almost equal. The pulse shapes recorded from the counters are analyzed to suppress the contribution from unwanted backgrounds.

The design of the proportional counters used is described in detail in Refs. [32, 40, 41]. The proportional counters, filled with  $\text{GeH}_4$  from each extraction, are placed in the well of a NaI veto detector within a large passive shield. To suppress the  $^{222}\text{Rn}$  background, the shield volume is purged with boil-off gas from the liquid nitrogen. The average counting time for the first four runs is approximately 50 d and was extended to about 140 d in the later six runs to account for the decreased source strength. Calibration data with an  $^{55}\text{Fe}$  source were taken once every 2 weeks throughout the measurements to ensure the stability of counting. Mean variations of the positions of the calibration peak during full counting period were 1.4% and 1.3% for the inner and the outer volumes and taken into account in analysis. Two periods during the counting were excluded from the analysis due to identified issues:

1. The time response of all slots in high-gain channel (L-peak) was slow between 2019-08-23 07:03 and 2019-09-14 14:49.
2. There was a failure in the low gain channel (K-peak) between 2019-11-06 21:10 and 2019-11-09 20:45.

The livetime of some runs were affected accordingly.

After the counting of the extraction samples from the Cr experiment was completed in the spring-fall of 2020, the counting efficiency was directly measured for each counter. The volume efficiencies, accounting for the dead volume near the cathode, were directly measured with  $^{37}\text{Ar}$ . The event selection efficiencies of the waveform analysis were measured with  $^{71}\text{Ge}$  calibrations. The rise-time ( $T_N$ ) values from the  $^{71}\text{Ge}$  calibration data were arranged in ascending order and an upper limit set such that 4% of the calibration events were excluded [25]. Details of the event selection and the  $^{71}\text{Ge}$  calibration runs

TABLE I. Extraction and exposure details for the inner target. The times of exposure are given in days of year 2019. A mass of  $(7.4691 \pm 0.0631)$  t of liquid Ga was irradiated by the neutrino source in the inner target.

Extraction		Source exposure		Solar exposure			Extraction efficiency	
Name	Date (2019)	Begin (day in year)	End (day in year)	Begin (day in year)	End (day in year)	Ga mass (tonnes)	from Ga	into GeH <sub>4</sub>
Inner-1	15 Jul 16:01	186.585	196.376	183.667	196.667	7.594	0.9747(97)	0.9460(123)
Inner-2	25 Jul 16:32	197.362	206.372	196.689	206.689	7.586	0.9814(98)	0.9559(124)
Inner-3	04 Aug 16:37	207.282	216.374	206.792	216.692	7.578	0.9795(98)	0.9673(126)
Inner-4	14 Aug 15:35	217.286	226.371	216.749	226.649	7.57	0.9801(98)	0.9515(124)
Inner-5	24 Aug 17:17	227.258	236.458	226.620	236.720	7.562	0.9808(98)	0.9554(124)
Inner-6	03 Sep 15:18	237.342	246.369	236.738	246.638	7.554	0.9818(98)	0.9548(124)
Inner-7	13 Sep 15:11	247.243	256.368	246.733	246.733	7.546	0.9813(98)	0.9381(122)
Inner-8	23 Sep 15:17	257.241	266.369	256.737	266.637	7.538	0.9835(98)	0.9789(127)
Inner-9	03 Oct 15:00	267.24	276.369	266.725	276.625	7.529	0.9824(98)	0.9545(123)
Inner-10	13 Oct 14:59	277.201	286.367	276.724	286.624	7.521	0.9806(98)	0.9372(122)

TABLE II. Extraction and exposure details for the outer target. The times of exposure are given in days of year 2019. A mass of  $(39.9593 \pm 0.0024)$  t of liquid Ga was irradiated by the neutrino source in the outer target.

Extraction		Source exposure		Solar exposure			Extraction efficiency	
Name	Date (2019)	Begin (day in year)	End (day in year)	Begin (day in year)	End (day in year)	Ga mass (tonnes)	from Ga	into GeH <sub>4</sub>
Outer-1	15 Jul 13:59	186.585	196.376	183.783	196.583	44.237	0.9868(99)	0.9503(124)
Outer-2	25 Jul 13:51	197.362	206.372	196.877	206.577	44.191	0.9841(98)	0.9581(125)
Outer-3	04 Aug 12:47	207.282	216.374	206.833	216.533	44.145	0.9881(99)	0.9668(126)
Outer-4	14 Aug 12:51	217.286	226.371	216.835	226.535	44.098	0.9858(99)	0.9622(125)
Outer-5	24 Aug 14:35	227.258	236.458	226.808	236.608	44.052	0.9871(99)	0.9609(125)
Outer-6	03 Sep 12:35	237.342	246.369	236.924	246.524	44.004	0.9893(99)	0.9253(120)
Outer-7	13 Sep 12:29	247.243	256.368	246.82	256.520	43.954	0.9904(99)	0.9514(124)
Outer-8	23 Sep 12:32	257.241	266.369	256.822	266.522	43.906	0.9897(99)	0.9897(129)
Outer-9	03 Oct 12:27	267.24	276.369	266.819	276.519	43.857	0.9881(99)	0.9664(126)
Outer-10	13 Oct 12:26	277.201	286.367	276.818	286.518	43.807	0.9877(99)	0.9538(124)

to verify the selection scheme are summarized in Sec. VB and Appx. A respectively.

The calculated counting efficiency using the measured pressure in the counter, GeH<sub>4</sub> fraction, and <sup>37</sup>Ar volume efficiency was determined for each extraction. They are summarized in Tables III and IV with other counting parameters. Values of the exponentially weighted livetime  $\Delta$  are also presented for each extraction

$$\Delta = \sum_{k=1}^n (e^{-\lambda t_{bk}} - e^{-\lambda t_{ek}}), \quad (1)$$

where the sum is over  $n$  counting intervals, each of which has a starting time  $t_{bk}$  and an ending time  $t_{ek}$ .  $\lambda$  is the decay constant of <sup>71</sup>Ge.

## V. ANALYSIS

A primary analysis on the BEST data was performed by the analysis group in the Institute for Nuclear Research, Russia, and was verified by an independent analysis carried out by a separate analysis group in Los Alamos National Laboratory. Both of the analyses obtained similar results to within about 2%. This difference is due to minor event-selection differences at the edges of the selection borders in energy and rise time. This difference is

accounted for by the estimated systematic uncertainties in the efficiencies for those cuts.

Pulses from the proportional counters are digitized at two different gains. The higher gain channel is chosen for the <sup>71</sup>Ge L-peak, and the lower gain channel is used for the K-peak analysis. The pulse shape analysis is performed to differentiate the <sup>71</sup>Ge signals from backgrounds.

The analytic form of pulse shapes used in the BEST analysis is derived from the model studied in Ref. [42] where

$$V(0 < t < T_N) = V_0 \left[ \frac{t+t_0}{T_N} \ln \left( 1 + \frac{t}{t_0} \right) - \frac{t}{T_N} \right],$$

$$V(t > T_N) = V_0 \left[ \ln \left( 1 + \frac{t-T_N}{t_0} \right) - 1 - \frac{t+t_0}{T_N} \ln \left( 1 - \frac{T_N}{t+t_0} \right) \right], \quad (2)$$

with  $V(t < 0) = 0$ . Here,  $T_N$  is the rise-time, which is the duration over which the ionization arrives at the anode,  $t_0$  is the time inversely proportional to the ion mobility, and  $V_0$  is the voltage proportional to the total amount of ionization. We fit every pulse that is not identified as saturation or breakdown to Eq. 2. The fit is made from 40 ns before the time of pulse onset to 400 ns after onset. Five parameters are determined by the fit:  $t_{\text{onset}}$ ,  $V_{\text{onset}}$ ,  $V_0$ ,  $t_0$ , and  $T_N$ . The integral of the fit function over pulse waveform for 800 ns after the onset is the energy parameter [24]. The  $T_N$  value is used as a background rejection parameter.

TABLE III. Counting parameters for the inner target.  $\Delta$  is the exponentially weighted live time. The live time and  $\Delta$  include all time cuts. The counter efficiency for each extraction has the same fractional uncertainty of  $-2.1/+2.3\%$ , as explained in details in Sec. V G.

Extraction		Counter filling		Counter efficiency (after event selection)		Day counting began (day in year)	Live time (days)		$\Delta$	
Run	Counter name	Pressure (mmHg)	GeH <sub>4</sub> fraction (%)	K-peak	L-peak		K-peak	L-peak	K-peak	L-peak
Inner-1	YCT92	630	8.8	0.3663	0.3803	197.66	54.478	34.364	0.8102	0.7450
Inner-2	YCT2	640	9.5	0.3647	0.3785	207.623	53.706	29.834	0.7839	0.6542
Inner-3	YCN43	650	9.3	0.3605	0.3599	217.693	50.525	50.525	0.7143	0.7143
Inner-4	YCT97	640	9.2	0.3679	0.3769	227.644	52.808	29.884	0.7872	0.3672
Inner-5	YCN46	650	9.5	0.3649	0.3654	237.790	150.436	150.436	0.7470	0.7470
Inner-6	YCN42	640	9.8	0.3577	0.3604	247.597	140.143	133.113	0.7717	0.3892
Inner-7	YCT92	640	9.3	0.3676	0.3793	257.617	129.483	130.843	0.7493	0.6776
Inner-8	YCT2	645	9.5	0.3656	0.3779	267.634	129.060	131.764	0.7754	0.7855
Inner-9	YCN43	640	9.1	0.359	0.3610	277.678	152.034	152.034	0.8019	0.8019
Inner-10	YCT97	650	9.1	0.3698	0.3755	287.625	144.446	147.014	0.7629	0.7955

TABLE IV. Counting parameters for the outer target.  $\Delta$  is the exponentially weighted live time. The live time and  $\Delta$  include all time cuts. The counter efficiency for each extraction has the same fractional uncertainty of  $-2.1/+2.3\%$ , as explained in details in Sec. V G.

Extraction		Counter filling		Counter efficiency (after event selection)		Day counting began (day in Year)	Live time (days)		$\Delta$	
Run	Counter Name	Pressure (mmHg)	GeH <sub>4</sub> fraction (%)	K-peak	L-peak		K-peak	L-peak	K-peak	L-peak
Outer-1	YCN113	635	9.5	0.3422	0.3596	197.66	53.788	33.662	0.7648	0.6996
Outer-2	YCT3	635	9.5	0.3707	0.3792	207.623	54.376	30.640	0.8043	0.6755
Outer-3	YCN49	640	10.5	0.2933	0.3358	217.693	51.070	51.070	0.7650	0.7650
Outer-4	YCT9	635	9.6	0.3658	0.381	227.644	52.981	30.423	0.7820	0.3755
Outer-5	YCN41	635	10.0	0.3568	0.3727	237.790	147.774	147.774	0.8025	0.8025
Outer-6	YCT4	630	9.0	0.3585	0.3577	247.597	139.382	131.148	0.8012	0.3843
Outer-7	YCN113	630	10.3	0.3407	0.3607	257.617	134.985	136.161	0.7977	0.7108
Outer-8	YCT3	640	9.5	0.3716	0.3785	267.634	129.098	131.802	0.8298	0.8398
Outer-9	YCN49	635	9.9	0.293	0.3360	277.678	155.439	155.439	0.7865	0.7865
Outer-10	YCT9	645	9.5	0.3677	0.3797	287.625	143.604	146.307	0.7567	0.7905

### A. Calibration

Following the procedure described in Ref. [24], we first find the position and the width of the 5.895 keV calibration peak in each calibration run. The expected locations for the <sup>71</sup>Ge K and L peaks are then calculated from the energy ratios with corrections for the non-linearity factors as described in Ref. [32]. For the counters with the GeH<sub>4</sub> fraction  $G$ , counter pressure  $P$ , and operating voltage  $V$ , the non-linearity factors for the location  $P_K$  and the resolution  $R_K$  of the K peak follow the empirical formulas reported in Ref. [32] as

$$\begin{aligned} \frac{P_K(^{71}\text{Ge})}{P(^{55}\text{Fe})} &= \frac{10.367}{5.895} [1 - (4.5G + 2.78)(V - V_{\text{crit1}}) \times 10^{-6}], \\ \frac{R_K(^{71}\text{Ge})}{R(^{55}\text{Fe})} &= \sqrt{\frac{5.895}{10.367}} [1 + 1.5 \times 10^{-3}(V - V_{\text{crit2}})], \end{aligned} \quad (3)$$

where the corrections are applied if  $V$  is above the respective critical voltages  $V_{\text{crit1}} = 10.5G + 0.6P + 588$  and

$V_{\text{crit2}} = 6G + P/3 + 824$ . The typical corrections for the K-peak position and the resolution are 2% and 15%, respectively, and no corrections are required for the L peak as the critical voltages are much higher than for the K peak.

We determine the proper energy scaling for each extraction from <sup>55</sup>Fe calibrations. The extrapolations were verified with <sup>71</sup>Ge filled counters operated after the BEST extraction counting ended. This additional study enabled the comparison between the <sup>71</sup>Ge K and L peak 2 FWHM regions predicted by extrapolation and the true peak positions. All counters used in the experiment underwent the performance study. Details of the counter calibration using <sup>71</sup>Ge isotope are described in Appx. A.

### B. Event selection

Events are further selected to reduce the background that mimics <sup>71</sup>Ge-induced events. The event selection algorithm uses the SAGE analysis [24], which has been

TABLE V. The cut values on  $T_N$  of the pulses for  $^{71}\text{Ge}$  K and L peak for each counting in the inner target. Events with  $T_N$  values greater than each cut value are selected out.

Counter Filling				$T_N$	
Extraction name	Counter name	Pressure (mmHg)	GeH <sub>4</sub> fraction (%)	K-peak (ns)	L-peak (ns)
Inner-1	YCT92	630	8.8	17.6	13.0
Inner-2	YCT2	640	9.5	16.6	10.1
Inner-3	YCN43	650	9.3	13.2	10.0
Inner-4	YCT97	640	9.2	17.3	11.4
Inner-5	YCN46	650	9.5	15.2	11.3
Inner-6	YCN42	640	9.8	13.2	9.1
Inner-7	YCT92	640	9.3	17.6	13.0
Inner-8	YCT2	645	9.5	16.6	10.1
Inner-9	YCN43	640	9.1	13.2	10.0
Inner-10	YCT97	650	9.1	17.3	11.4

TABLE VI. The cut values on  $T_N$  of the pulses for  $^{71}\text{Ge}$  K and L peak for each counting in the outer target. Events with  $T_N$  values greater than each cut value are selected out.

Counter Filling				$T_N$	
Extraction name	Counter name	Pressure (mmHg)	GeH <sub>4</sub> fraction (%)	K-peak (ns)	L-peak (ns)
Outer-1	YCN113	635	9.5	13.6	9.1
Outer-2	YCT3	635	9.5	16.4	10.3
Outer-3	YCN49	640	10.5	18.8	13.2
Outer-4	YCT9	635	9.6	14.9	9.1
Outer-5	YCN41	635	10.0	13.4	10.3
Outer-6	YCT4	630	9.0	13.2	10.2
Outer-7	YCN113	630	10.3	13.6	9.1
Outer-8	YCT3	640	9.5	16.4	10.3
Outer-9	YCN49	635	9.9	18.8	13.2
Outer-10	YCT9	645	9.5	14.9	9.1

continuously updated throughout the last 20 years. Some of the updates were reported in [41].

We implement five event selection cuts to remove non-physical signals: 1) flatness cut, 2) shield-open cut, 3) NaI veto cut, 4) setting the energy windows for the Ge L and K peaks and 5) rise-time cut. These cuts effectively remove the background events. The first three types of cuts affects only the background level of the counters, and do not affect the selection of real events from  $^{71}\text{Ge}$  decays. Therefore the efficiency of such cuts can be considered equal to 100%. The use of such cuts off reduces the background of the counters and, accordingly, the magnitude of the statistical error.

### 1. Flatness cut

The first step of event selection is to identify two types of background events: saturation waveforms that are mostly from high energy  $\alpha$ -particles and those that originate from high-voltage breakdown. The  $\alpha$ -particles, either from the decay of internal  $^{222}\text{Rn}$  or the natural radioactivity in the counter material, can easily be identified by examining the end of the waveforms. Saturated

pulses have amplitudes greater than 16 keV and relatively flat shape at the end of the pulse. The events from high-voltage breakdown have a characteristic waveform that rises steeply and stays flat at the end. While the positive ions from the real  $^{71}\text{Ge}$  events are collected smoothly over time with resulting extended rise time, events from high-voltage breakdown have a characteristic waveform that rises steeply and stays flat at the end after the rising edge. Because both types of background events have a characteristic shape at the end of the waveform, we analyze the pulses between 500 and 1000 ns after the digitization begins. Typical waveforms of an  $\alpha$ -induced saturated pulse and a background that originates from high-voltage breakdown are shown in Fig. 3. They are easily distinguishable from the typical pulse shape of true  $^{71}\text{Ge}$  candidate event shown in Fig. 4.

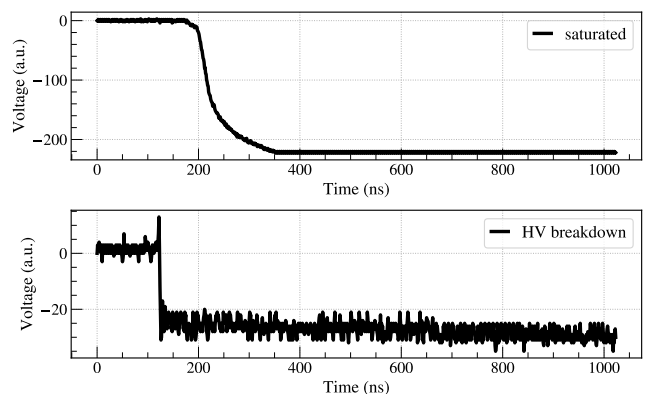


FIG. 3. Flat-top pulses measured in proportional counters. **Top:** Saturated event induced by high-energy  $\alpha$ -particles. **Bottom:** Background candidate event that originates from high-voltage breakdown.

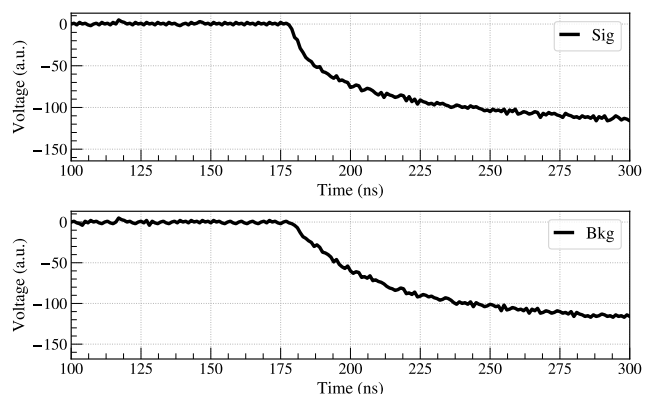


FIG. 4. Typical pulse shapes measured in proportional counters. **Top:**  $^{71}\text{Ge}$  K peak candidate event with  $T_N = 7.44$  ns. **Bottom:** Background candidate event induced by either Compton scattering or high-energy  $\beta$ -particles in K peak energy region. The slow background event with extended ionization has much slower fall time ( $T_N = 30.67$  ns) when the pulse begins at  $\approx 200$  ns than the true  $^{71}\text{Ge}$  candidate event.

## 2. Shield-open cut

Next, we apply a cut to remove data during periods of expected high backgrounds. When counters were calibrated, they were exposed to the laboratory atmosphere with an average Rn content of 2 pCi/liter. Events produced by  $^{222}\text{Rn}$  daughters can produce false  $^{71}\text{Ge}$  signals that mimic our signal, and hence the effect of external Rn is minimized by making a time cut on the data for 2.6 h after any shield opening. The estimated effectiveness of this time cut is nearly 100%. Any rejected period are considered in our exposure calculation, and there is no efficiency associated with it. The uncertainty is found to be negligible [43].

## 3. Time cut of Radon chains

We apply an additional time cut to minimize the number of false  $^{71}\text{Ge}$  signals from internal radon and its daughters [32]. The first two decays in the  $^{222}\text{Rn}$  chain are  $\alpha$  decays producing off-scale pulses that saturate the detector. Since  $^{222}\text{Rn}$  decays to  $^{210}\text{Pb}$  ( $T_{1/2} = 22\text{-y}$ ) typically in about an hour, removing a few hours around each saturated event effectively rejects the false  $^{71}\text{Ge}$  events from the radon chain. We remove all data from 15 minutes before each saturation event to 3 hours after it [32, 41]. The probability that the decays of the elements of this chain will be registered after such cut off is 1.1% for  $^{214}\text{Pb}$  and 3.5% for  $^{214}\text{Bi}$  and  $^{214}\text{Po}$  [44]. We treat them as the systematic uncertainties related to internal radon.

## 4. NaI veto

Background events from  $\beta$  decays from the counter walls, which are accompanied by  $\gamma$  rays are tagged and vetoed by the surrounding NaI detector. Since  $^{71}\text{Ge}$  has no  $\gamma$  rays associated with its decay other than internal bremsstrahlung, all events coincident with a NaI detector response are eliminated.

## 5. Setting the energy windows for the Ge L and K peaks

The measure of energy is the integral of the pulse waveform for 800 ns after the pulse onset. The locations of the energy acceptance windows for  $^{71}\text{Ge}$  events in the L and K peaks were set from the  $^{55}\text{Fe}$  calibration as described in Sec. V A. If the peak position changes from one calibration to the next, then the energy window for event selection is slid linearly in time between the two calibrations. The resolution at each peak is held constant and is set to be the average of the resolutions of  $^{55}\text{Fe}$  for all counter calibrations, scaled to the L- or K-peak energy as described in Sec. V A. Events are then accepted as can-

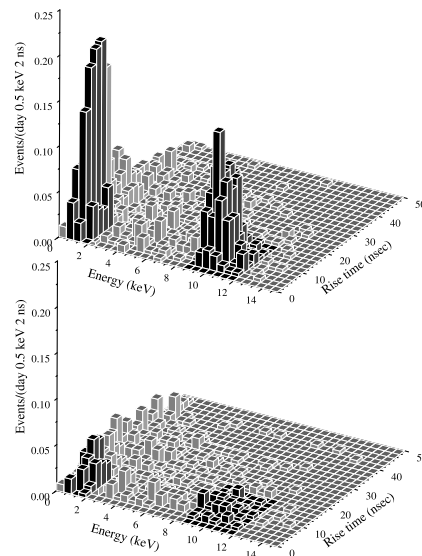


FIG. 5. **Upper panel:** energy vs rise-time histogram of all events of the inner target after the shield-open cut observed in all ten exposures during the first 30 days after extraction. The live time is 245 days, and 1364 events are shown. **Lower panel:** the same histogram for the 481 events that occurred during an equal live-time interval beginning at 40 days after extraction.

didates only if their energy is within  $\pm 1$  FWHM ((98% acceptance) of the central peak energy.

## 6. Rise-time cut

The electron capture process produces point-like ionization in the counter. Pulses from the  $^{71}\text{Ge}$  electron capture decay should therefore be fast, and  $T_N$  values should be near zero. On the other hand, backgrounds from Compton scattering or from high-energy  $\beta$ -particles traversing the counter produce extended ionizations, leading to slow pulses with large  $T_N$ . Figure 4 illustrates the difference in pulse shapes of the point-like  $^{71}\text{Ge}$  candidate event with  $T_N = 7.44$  ns and the background showing the characteristic of extended ionization with  $T_N = 30.67$  ns. Both events fall into the K peak energy region with 9.64 keV, but the background candidate event has much slower fall time when the pulse begins at  $\approx 200$  ns than the true  $^{71}\text{Ge}$  candidate.

The cut value for the  $T_N$  for each counter is obtained from separate measurements by filling counters with a typical gas mixture (see Tables V and VI) and adding a trace of active  $^{71}\text{GeH}_4$ . The counters were filled with a mixture ( $\% \text{GeH}_4 \sim 10\%$  and pressure  $\approx 650$  mmHg) very similar to the mixture used in the BEST extractions. Each proportional counter was installed into the same

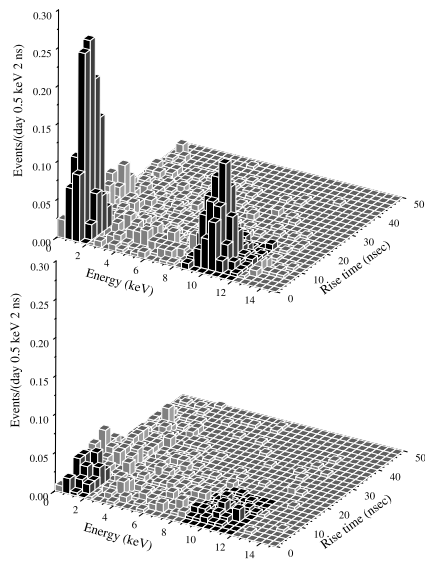


FIG. 6. **Upper panel:** energy vs rise-time histogram of all events of the outer target after the shield-open cut observed in all ten exposures during the first 30 days after extraction. The live time is 249 days, and 1387 events are shown. **Lower panel:** the same histogram for the 504 events that occurred during an equal live-time interval beginning at 40 days after extraction.

TABLE VII. A summary of event selection cuts and their individual acceptances.

Cut	Efficiency (%)
Energy window	$98 \pm 1.3$
Rise-time	96

channel of the counting system with approximately the same high voltage as used in the BEST measurements. The cut values for the K and L peaks are set such that 4% of the slowest events in  $^{71}\text{Ge}$  calibration data are excluded. The derived typical cut values for K and L peaks were 13.2 ns and 9.1 ns respectively. However, the cut values vary by detector, and individual  $T_N$  values were used for each counter. The cut values on  $T_N$  windows for K and L peak for each counter are given in Tables V and VI.

Table VII summarizes the event selection cuts applied in the BEST analysis and their individual acceptances. Figures 5 and 6 show the histograms of all events from the inner and the outer zones, after the first four cuts, for the earlier and the later counting times. The number of events outside the peaks is about the same in both panels as these are mainly due to background. The expected location of the  $^{71}\text{Ge}$  K and L peaks as predicted by the

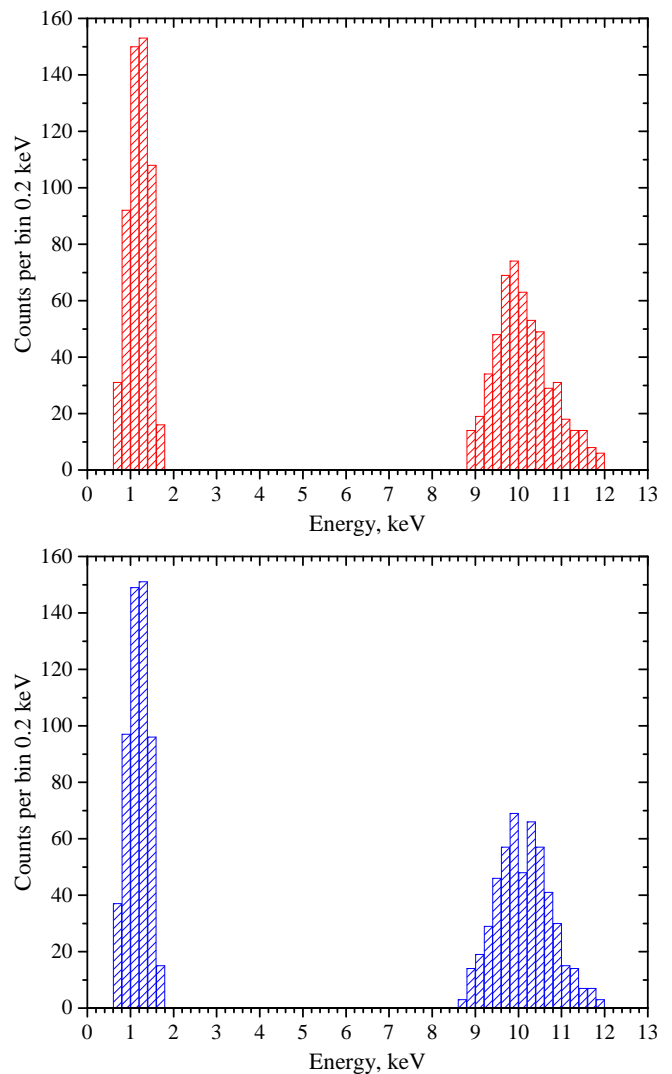


FIG. 7. Plots with energy spectra of selected events for whole dataset showing K and L peaks. **Top:** Energy spectrum of the inner target. **Bottom:** Energy spectrum of the outer target.

$^{55}\text{Fe}$  calibrations are shown as darkened.

Figure 7 shows the energy spectra of the selected K and L peak candidate events for the inner and the outer targets. We note that the event selection windows were determined from post-experiment calibrations, and hence the cut boundary parameters were effectively blind during the analysis. No additional blindness scheme was implemented.

### C. Neutrino-Nucleon Cross Section

The neutrino-nucleon cross section ( $\sigma$ ) has to be calculated from nuclear physics input. The bulk of the cross section is in the ground-state to ground-state transition determined from the matrix element for the decay of

TABLE VIII. A summary of the published neutrino-nucleon cross section estimates for  $^{71}\text{Ge}$  in units of  $10^{-45}\text{cm}^2$ .

Reference	Cross Section	Q-value (keV)
[45]	$5.81^{+0.21}_{-0.16}$	232.69(15)
[49]	$5.93\pm 0.14$	232.69(15)
[51]	$5.910\pm 0.114$	233.5(1.2)
[52]	$5.67\pm 0.06$	232.49(22)
[53]	$5.938\pm 0.116$	232.443(93)

$^{71}\text{Ge}$ . When the original gallium anomaly was observed, there was concern that the transition strengths to excited states were not fully understood. The cross section was first estimated in the seminal work of Bahcall [45]. He derived the ground state contribution from the  $^{71}\text{Ge}$  half-life, but the excited state contributions were estimated from charge exchange (i.e. (p,n)) reactions. Bahcall considered a number of possible uncertainties, the largest coming from the excited state contributions due to the quality of the (p,n) data available at that time. For the central value, Bahcall used the best estimate of the transition strength values to the first two excited states and a Q-value of  $(232.69\pm 0.15)$  keV. Other excited states are too high in energy to contribute for  $^{51}\text{Cr}$   $\nu$ 's energy. Bahcall estimated the uncertainty to be the change in  $\sigma$   $(-1.6/+2.8\%)$  if one ignores the excited states. Other uncertainties came from forbidden corrections to the beta decay matrix elements (2.3%) with small uncertainties associated with the  $Q_{val}$  (0.05%), the reaction threshold (0.2%), and the  $^{71}\text{Ge}$  half life (0.3%). He considered part of the excited state uncertainty as one-sided, hence the asymmetric uncertainties. The charge exchange data has been improved [46] by recent work [47–49] indicating that they are not the cause of the discrepancy. However, the excited-state contribution uncertainty is critical because the (p,n) measurements have a significant cancellation between the Gamow-Teller and tensor matrix elements resulting in an underestimate of the transition strengths [50]. The (p,n) cross section could be entirely due to the tensor interaction, in which case (either) excited state contribution to neutrino absorption might be zero. Unfortunately, there is no direct measurement of the cross section at this energy that is not subject to the caveats of neutrino oscillation physics.

Kostensalo *et al.* [52] used a more recent  $Q_{val} = (232.49 \pm 0.22)$  keV [54] and a nuclear shell model calculation with wave functions obtained using recent two-nucleon interactions to calculate the transition strengths. The shell model calculations thus avoid the drawback of using the (p,n) measurements but need to be experimentally confirmed by indirect means, such as state energies and electromagnetic properties. The paper of Semenov *et al.* [53] reproduces Bahcall's approach but uses modern values for the transition strengths and a Q-value of  $(232.443\pm 0.093)$  keV [55]. This small difference in Q-value between the estimates generates a small uncer-

tainty compared to the other uncertainties in this work and we ignore it.

The Semenov *et al.* and Kostensalo *et al.* results differ by about 4%, which is about 2-3 times larger than the uncertainty estimated for each. Interestingly, the original Bahcall number is half way between these two results with a  $\pm 4\%$  uncertainty. We therefore use the Bahcall  $\sigma$  value and the associated conservative uncertainties from his estimate of  $[(5.81^{+0.21}_{-0.16}) \times 10^{-45}] \text{cm}^2$ . The recent cross section estimates are summarized in Table VIII.

#### D. Energy-weighted Likelihood Fits

The time sequence of the candidate  $^{71}\text{Ge}$  events are analyzed with a maximum likelihood method to separate the  $^{71}\text{Ge}$  decay with 11.4 day half-life from remaining background, which is constant over time. The likelihood fit takes into account the decay of  $^{51}\text{Cr}$  during the exposure period.

In general, the likelihood function ( $\mathcal{L}$ ) used in the BEST analysis can be written for a single run as

$$\mathcal{L} = e^{-\int_{\text{counting time}} P(t,E)dt} \prod_i^l P(t_i, E_i) dt_i, \quad (4)$$

where  $l$  is the total number of observed events,  $t_i$  is the time of event  $i$ , and  $P(t, E)$  is the total probability that an event with energy  $E$  will occur at time  $t$ . If the events that pass all selection criteria are classified as either the signal or the background, the function  $P(t, E)$  can be generalized to the form

$$P(t, E) = w_p(E)p\epsilon e^{-\lambda t} + w_b(E)b, \quad (5)$$

where  $p$  and  $b$  are the production rate and the background rate, respectively;  $\epsilon$  is the overall efficiency; and the terms  $w_p(E)$  and  $w_b(E)$ , called the weight factors, are the energy-dependent probabilities that the event is due to signal or to background, respectively. The functional form of  $w_p(E)$  must be obtained from an experiment in which only signal is present, and the form of  $w_b(E)$  is measured when only background is present. It is assumed that both weight factors are independent of time and are normalized such that

$$\int_{E_{lo}}^{E_{hi}} w_p(E)dE = \int_{E_{lo}}^{E_{hi}} w_b(E)dE = 1, \quad (6)$$

where the integrals extend over the range  $E_{lo}$  to  $E_{hi}$  used in event selection ( $\pm 1$  FWHM for this analysis).

Combining Eq. 4, 5 and 6, the likelihood function is generalized to

$$\mathcal{L} = e^{-p\epsilon\Delta/\lambda - b\tau} \prod_i^l [w_p(E_i)p\epsilon e^{-\lambda t_i} + w_b(E_i)b] dt_i dE_i, \quad (7)$$

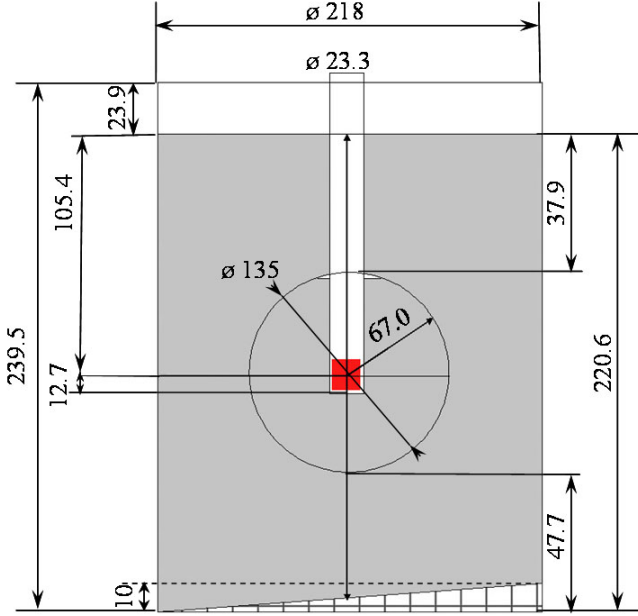


FIG. 8. The geometrical dimensions of the Ga targets. All dimensions are in centimeters. There is an empty segment in the spherical vessel due to the thickened wall and the bottom of the re-entrant tube.

where  $\Delta$  is the probability an event will occur while counting is in progress and  $\tau$  is the total counting time. For maximization purposes, the likelihood function can be arbitrary up to a constant. Hence, Eq. 7 can be divided by  $\prod_i^l w_b(E_i) dt_i dE_i$  and written as

$$\mathcal{L} = e^{-p\epsilon\Delta/\lambda - b\tau} \prod_i^l \left[ \frac{w_p(E_i)}{w_b(E_i)} p\epsilon e^{-\lambda t_i} + b \right], \quad (8)$$

which is the standard function that is used by all radiochemical solar neutrino experiments to analyze their counting data where the usual term  $e^{-\lambda t_i}$  has been replaced by

$$\frac{w_p(E_i)}{w_b(E_i)} e^{-\lambda t_i}. \quad (9)$$

The signal and the background weight factors were determined by examining the energy spectra for each counter. The use of the energy weight factors shifts the results by values that are quite compatible with the statistical uncertainty.

### E. Predicted $^{71}\text{Ge}$ Production Rates

The expected  $^{71}\text{Ge}$  production rates depend on various physical constants presented in Table IX and the geometries of the targets, illustrated in Fig. 8. To account

for the non-trivial shapes of the Ga targets, a Monte Carlo integration technique was adapted for the neutrino capture rate calculations in the target zones. Calculations with the nominal geometry described in Fig. 8 yield  $1.22545 \text{ m}^3$  and  $6.5561 \text{ m}^3$ , which correspond to  $7.4691 \text{ t}$  and  $39.9593 \text{ t}$  of liquid Ga. The measured masses of the targets are  $7.4060 \text{ t}$  and  $39.9617 \text{ t}$  for the inner and outer zones, respectively, with negligible uncertainty for both masses.

We attribute the discrepancy of the measured and the calculated mass values to the uncertainty in the dimensional measurements, especially in the shell thickness of the spherical volume. In a study to explore how sensitive the Monte Carlo results are to various alterations in geometry, modifying the spherical shell thickness from the nominal value of  $0.50 \text{ cm}$  to  $0.68 \text{ cm}$  was found to neutralize the difference in the mass values. We include the error of inaccurate knowledge of the sphere shell thickness as a systematic uncertainty of the path length, which for the sphere amounts to  $0.4\%$  and for the cylinder is negligible. Accounting also for the uncertainties in gallium weighing, we use  $(7.4691 \pm 0.0631) \text{ t}$  and  $(39.9593 \pm 0.0024) \text{ t}$  as the nominal masses of the inner and the outer targets.

The effective path length in a volume, or the average path length the  $\nu_e$  takes through the Ga target, is calculated by the integral

$$\langle L \rangle = \int_V \frac{1}{4\pi d^2} d\vec{x}, \quad (10)$$

where  $d$  is the distance between emission in the source and absorption in the Ga targets

We carry out the Monte Carlo integration to yield the path length values for the inner and the outer volumes. Taking into account both the statistical uncertainty due to the  $10^7$  sample Monte Carlo integration and the systematic uncertainty from the dimensional uncertainties of the apparatus, the average path lengths for the two volumes are

$$\begin{aligned} \langle L \rangle_{in} &= (52.03 \pm 0.18) \text{ cm}, \text{ and} \\ \langle L \rangle_{out} &= (54.41 \pm 0.18) \text{ cm}. \end{aligned} \quad (11)$$

The neutrino capture rate  $r_j$  in the volume  $V_j$  can be written as

$$\begin{aligned} r_j &= \sum_k^4 \int_{V_j} F P_{ee}(\vec{x}, E_{\nu_k}) \sigma_k n d\vec{x} \\ &\approx V_0 \frac{1}{N} \sum_k^4 \sum_{i=1}^N \frac{p_k P_{ee}(d, E_{\nu_k})}{d^2} \Theta_j(\vec{x}_i), \end{aligned} \quad (12)$$

where  $F$  is the flux of  $\nu_e$ ,  $P_{ee}(\vec{x}, E_{\nu_k})$  is the oscillation survival probability of  $\nu_e$  with energy  $E_{\nu_k}$ ,  $p_k$  is the branching ratio for the  $\nu_e$  with energy  $E_{\nu_k}$ ,  $\sigma_k$  is the cross section,  $n$  is the  $^{71}\text{Ga}$  number density, and  $\Theta(\vec{x}_i) = 1$  if  $\vec{x}_i$

TABLE IX. Values and uncertainties of the terms that enter the calculation of the predicted production rate. All uncertainties are symmetric except for the cross section.

	Value	Uncertainty	
		Magnitude	%
Ga density $\rho$ (g Ga/cm <sup>3</sup> )	6.095	0.002	0.033
Avogadro's number $N_0$ (10 <sup>23</sup> atoms Ga/mol)	6.0221	0.0	0.0
Ga molecular weight $M$ (g Ga/mol)	69.72307	0.00013	0.0002
<sup>71</sup> Ga Atomic abundance $f_1$ (atoms <sup>71</sup> Ga/100 atoms Ga) [56]	39.8921	0.0062	0.016
Atomic density $D = \rho N_0 f_1 / M$ (10 <sup>22</sup> atoms <sup>71</sup> Ga/cm <sup>3</sup> )	2.1001	0.0008	0.037
Source activity at reference time $A$ , MCi	3.414	0.008	0.23
Cross section $\sigma$ (10 <sup>-45</sup> cm <sup>2</sup> / ( <sup>71</sup> Ga atom <sup>51</sup> Cr decay)), Bahcall	5.81	+0.21,-0.16	+3.6,-2.8
Path length in Ga $\langle L_{in} \rangle$ (cm)	52.03	0.18	0.3
Path length in Ga $\langle L_{out} \rangle$ (cm)	54.41	0.18	0.3
Predicted production rate ( <sup>71</sup> Ge atoms/d), $r_{In}$	69.4	+2.5,-2.0	+3.6,-2.8
Predicted production rate ( <sup>71</sup> Ge atoms/d), $r_{Out}$	72.6	+2.6,-2.1	+3.6,-2.8

is within  $V$  and 0 otherwise. The summation over  $k$  is for the four neutrino energies and their branching ratios 747 keV (81.63%), 427 keV (8.95%), 752 keV (8.49%) and 432 keV (0.93%) [31]. The summation over  $i$  is for the Monte Carlo integration over  $N$  samples. For the no oscillation case, the survival probability at a short distance is simply  $P_{ee}(d) = 1$ . In the case where only one sterile mass eigenstate  $m_4$  is introduced to the standard three active mass states and  $m_4 \gg m_1, m_2, m_3$ , the survival probability of any active neutrino at a short distance  $d$  is governed by the two-neutrino oscillation model

$$P_{ee}(E_\nu, d) = 1 - \sin^2 2\theta \sin^2 \left( 1.27 \frac{\Delta m^2 [\text{eV}^2] d [\text{m}]}{E_\nu [\text{MeV}]} \right), \quad (13)$$

where  $\Delta m^2$  is the mass squared difference between the active and the inactive state,  $\theta$  is the mixing angle, and  $E_\nu$  is the neutrino energy.

Using the source activity of (3.414±0.008) MCi, the neutrino-nucleus cross section, and combining the uncertainty in quadrature, Eq. 12 gives the predicted production rates of

$$\begin{aligned} r_{\text{In-predic}} &= (69.4^{+2.5}_{-2.0}) \text{ atom/d}, \\ r_{\text{Out-predic}} &= (72.6^{+2.6}_{-2.1}) \text{ atom/d}. \end{aligned} \quad (14)$$

The uncertainties are dominated by the cross-section uncertainty, and thus are strongly correlated in these predictions for the two volumes.

## F. Measured <sup>71</sup>Ge Production Rates

The results of the likelihood fits for individual runs and the combined fits are presented in Tables X and XI. For each run and also for the combined runs, the likelihood fits to the time distribution of the candidate events were performed as described in Refs. [24, 25].

The background from solar neutrino capture conforms to (66.1±3.1) solar neutrino unit (SNU<sup>1</sup>) [41] as explained below, and was taken into account when determining the production rate from the source. In general, the contribution from the solar neutrino capture is 0.6 and 3.2 counts for the inner and the outer targets. These are 0.8% and 4.6% of the total numbers fit to <sup>71</sup>Ge, respectively. Due to the inefficiency of extractions, there are also residual <sup>71</sup>Ge atoms that carryover from one extraction to the next. The contribution from the carryover atom was typically less than 1 count for each volume and was also taken into account.

The best fit production rates of <sup>71</sup>Ge from the combined data analysis for each target at the reference time are

$$\begin{aligned} r_{\text{In-fit}} &= (54.9 \pm 2.5) \text{ atoms/d}, \\ r_{\text{Out-fit}} &= (55.6 \pm 2.7) \text{ atoms/d}. \end{aligned} \quad (15)$$

The stated uncertainty is statistical and is given with 68% confidence. The fit values of <sup>71</sup>Ge half-life from the inner and the outer targets are (11.11 ± 0.69) d and (11.05 ± 0.72) d. These are in good agreement with the accepted half-life of (11.43 ± 0.03) d [39].

## G. Systematic Studies

The systematic uncertainties are categorized into four basic types: 1) uncertainties related to the chemical extraction efficiency ( $\delta_G$ ), 2) uncertainties in the counting efficiency ( $\delta_C$ ), 3) uncertainties arising from background phenomena ( $\delta_N$ ), and the average path length uncertainty. The uncertainties related to the measurement are summarized in Table XII, while item 4) is related to the prediction.

<sup>1</sup> 1 SNU = 1 interaction per 10<sup>36</sup> target atoms per second

TABLE X. A summary of the likelihood fits for the production rate for the inner target from each extraction and the combined fit of all extractions, in K and L peak independently and combined. The production rates for each exposure for the K and L-peaks are referred to its starting time, taking into account the total detection efficiency. The production rate for their combined result is referred to the reference time. All production rates for the K+L-peak are referred to the reference time. The stated uncertainties are statistical and given in 68% confidence. The Cramér-von Mises statistics  $Nw^2$  measures the goodness of fit of the sequence of event times. The probability was inferred from  $Nw^2$  by simulation.

## K-peak

Extraction	Number of candidate events	Number fit to $^{71}\text{Ge}$	$^{51}\text{Cr}$ source production	Solar $\nu$ production	Carryover	$^{71}\text{Ge}$ Production decay rate (atoms/day)	$Nw^2$	Probability (%)
Inner-1	88	88.0	87.6	0.4	0.0	$48.2^{+6.3}_{-4.2}$	0.110	49
Inner-2	81	70.2	68.1	0.4	1.7	$40.5^{+5.6}_{-6.8}$	0.081	58
Inner-3	69	61.2	60.1	0.3	0.8	$39.0^{+5.9}_{-6.1}$	0.124	35
Inner-4	65	65.0	63.9	0.3	0.8	$37.5^{+5.6}_{-4.2}$	0.057	82
Inner-5	57	32.5	31.6	0.3	0.6	$19.5^{+3.6}_{-4.6}$	0.107	23
Inner-6	44	36.4	35.7	0.2	0.5	$22.0^{+3.7}_{-4.4}$	0.026	96
Inner-7	43	23.0	22.4	0.3	0.3	$14.0^{+3.1}_{-3.9}$	0.048	70
Inner-8	28	15.9	15.3	0.3	0.3	$8.9^{+2.6}_{-3.3}$	0.160	11
Inner-9	40	6.3	5.8	0.3	0.2	$3.4^{+2.0}_{-2.9}$	0.071	54
Inner-10	28	13.3	12.9	0.3	0.1	$7.8^{+2.3}_{-3.0}$	0.031	91
Comb. K	543	411.6	403.2	3.0	5.4	$58.5^{+3.4}_{-3.5}$	0.095	44

## L-peak

Extraction	Number of candidate events	Number fit to $^{71}\text{Ge}$	$^{51}\text{Cr}$ source production	Solar $\nu$ production	Carryover	$^{71}\text{Ge}$ Production decay rate (atoms/day)	$Nw^2$	Probability (%)
Inner-1	92	89.5	89.2	0.4	0.0	$51.4^{+8.3}_{-4.1}$	0.353	6
Inner-2	48	42.5	40.8	0.4	1.4	$28.0^{+5.2}_{-5.7}$	0.023	99
Inner-3	63	56.2	55.1	0.3	0.8	$35.8^{+6.1}_{-5.8}$	0.079	58
Inner-4	28	19.5	19.0	0.2	0.3	$23.3^{+6.2}_{-7.4}$	0.101	36
Inner-5	77	27.5	26.6	0.3	0.6	$16.4^{+3.4}_{-4.6}$	0.046	74
Inner-6	37	11.6	11.2	0.2	0.2	$13.7^{+4.6}_{-6.0}$	0.115	20
Inner-7	48	22.1	21.5	0.3	0.3	$14.4^{+3.5}_{-4.5}$	0.142	9
Inner-8	31	17.6	17.0	0.3	0.3	$9.4^{+2.3}_{-3.1}$	0.066	53
Inner-9	66	17.4	16.9	0.3	0.2	$9.9^{+2.9}_{-3.7}$	0.209	5
Inner-10	60	11.4	11.0	0.3	0.2	$6.3^{+2.4}_{-3.2}$	0.085	44
Comb. L	550	311.3	304.0	3.0	4.3	$50.7^{+3.7}_{-3.7}$	0.07	48

## K+L-peak

Extraction	Number of candidate events	Number fit to $^{71}\text{Ge}$	$^{51}\text{Cr}$ source production	Solar $\nu$ production	Carryover	$^{71}\text{Ge}$ Production decay rate (atoms/day)	$Nw^2$	Probability (%)
Inner-1	180	176.3	175.5	0.8	0.0	$49.4^{+4.0}_{-4.2}$	0.398	6
Inner-2	129	111.5	107.7	0.8	3.1	$44.9^{+5.6}_{-5.9}$	0.065	70
Inner-3	132	117.6	115.3	0.7	1.6	$62.9^{+7.1}_{-7.4}$	0.056	76
Inner-4	93	87.3	85.6	0.6	1.1	$73.3^{+8.0}_{-8.6}$	0.077	59
Inner-5	134	60.2	58.4	0.6	1.2	$49.8^{+7.7}_{-8.2}$	0.033	92
Inner-6	81	48.8	47.7	0.4	0.7	$69.5^{+11.0}_{-12.0}$	0.067	49
Inner-7	91	45.0	43.9	0.5	0.6	$64.6^{+11.6}_{-12.6}$	0.127	13
Inner-8	59	33.6	32.4	0.6	0.6	$53.8^{+11.0}_{-12.2}$	0.037	87
Inner-9	106	23.7	22.7	0.6	0.4	$49.9^{+14.9}_{-16.5}$	0.164	10
Inner-10	88	25.2	24.3	0.6	0.3	$69.1^{+17.3}_{-19.4}$	0.108	26
Comb. K+L	1093	724.0	708.2	6.1	9.7	$54.9^{+2.4}_{-2.5}$	0.099	28

TABLE XI. A summary of the likelihood fits for the production rate for the outer target from each extraction and the combined fit of all extractions, in K and L peak independently and combined. The production rates for each exposure for the K and L-peaks are referred to its starting time, taking into account the total detection efficiency. The production rate for their combined result is referred to the reference time. All production rates for the K+L-peak are referred to the reference time. The stated uncertainties are statistical and given in 68% confidence. The Cramér-von Mises statistics  $Nw^2$  measures the goodness of fit of the sequence of event times. The probability was inferred from  $Nw^2$  by simulation.

## K-peak

Extraction	Number of candidate events	Number fit to $^{71}\text{Ge}$	$^{51}\text{Cr}$ source production	Solar $\nu$ production	Carryover	$^{71}\text{Ge}$ Production decay rate (atoms/day)	$Nw^2$	Probability (%)
Outer-1	89	77.3	75.4	1.8	0.1	$46.8^{+6.1}_{-7.5}$	0.051	83
Outer-2	99	89.1	86.3	1.8	1.0	$49.1^{+5.1}_{-7.5}$	0.070	67
Outer-3	62	48.1	46.1	1.3	0.7	$34.3^{+5.7}_{-8.2}$	0.158	20
Outer-4	64	55.2	53.0	1.7	0.5	$31.2^{+4.6}_{-6.1}$	0.037	90
Outer-5	50	28.4	26.2	1.7	0.5	$15.3^{+2.5}_{-5.0}$	0.148	9
Outer-6	50	43.6	41.6	1.6	0.4	$25.4^{+3.1}_{-5.4}$	0.085	53
Outer-7	28	20.5	18.7	1.6	0.2	$11.6^{+1.7}_{-4.2}$	0.227	6
Outer-8	33	25.0	22.9	1.9	0.2	$12.1^{+1.7}_{-4.0}$	0.130	25
Outer-9	23	10.6	9.1	1.4	0.1	$6.6^{+0.0}_{-4.0}$	0.055	63
Outer-10	27	16.7	14.9	1.7	0.1	$9.0^{+1.6}_{-4.0}$	0.043	78
Comb. K	524	415.4	395.1	16.6	3.7	$59.4^{+3.6}_{-3.7}$	0.066	58

## L-peak

Extraction	Number of candidate events	Number fit to $^{71}\text{Ge}$	$^{51}\text{Cr}$ source production	Solar $\nu$ production	Carryover	$^{71}\text{Ge}$ Production decay rate (atoms/day)	$Nw^2$	Probability (%)
Outer-1	92	51.5	49.6	1.8	0.1	$32.1^{+6.9}_{-9.1}$	0.216	11
Outer-2	75	75.0	72.6	1.5	0.9	$48.1^{+7.5}_{-4.9}$	0.035	95
Outer-3	54	45.9	43.6	1.5	0.8	$28.4^{+4.2}_{-6.2}$	0.202	15
Outer-4	34	27.0	25.9	0.8	0.3	$30.4^{+6.0}_{-8.5}$	0.159	18
Outer-5	70	35.6	33.3	1.8	0.5	$18.6^{+2.6}_{-5.3}$	0.045	74
Outer-6	47	18.3	17.3	0.8	0.2	$22.1^{+5.1}_{-8.1}$	0.147	9
Outer-7	41	17.2	15.5	1.5	0.2	$10.2^{+2.1}_{-4.6}$	0.071	47
Outer-8	35	18.0	15.9	1.9	0.2	$8.1^{+1.4}_{-3.8}$	0.060	58
Outer-9	43	9.1	7.3	1.7	0.1	$4.6^{+1.5}_{-4.0}$	0.080	44
Outer-10	54	14.6	12.6	1.9	0.1	$7.1^{+1.6}_{-4.0}$	0.038	85
Comb. L	545	320.6	302.0	15.3	3.3	$50.9^{+3.9}_{-3.9}$	0.062	54

## K+L-peak

Extraction	Number of candidate events	Number fit to $^{71}\text{Ge}$	$^{51}\text{Cr}$ source production	Solar $\nu$ production	Carryover	$^{71}\text{Ge}$ Production decay rate (atoms/day)	$Nw^2$	Probability (%)
Outer-1	181	133.4	129.6	3.7	0.1	$41.1^{+5.2}_{-5.3}$	0.191	18
Outer-2	174	163.8	158.6	3.3	1.9	$63.6^{+5.5}_{-5.7}$	0.065	73
Outer-3	116	92.5	88.2	2.8	1.5	$51.4^{+6.9}_{-7.3}$	0.123	32
Outer-4	98	82.3	78.9	2.5	0.8	$66.6^{+9.2}_{-9.8}$	0.045	84
Outer-5	120	64.0	59.5	3.5	1.0	$46.9^{+7.2}_{-7.9}$	0.068	48
Outer-6	97	62.3	59.3	2.6	0.4	$87.3^{+12.3}_{-13.2}$	0.095	30
Outer-7	69	38.0	34.4	3.2	0.4	$50.4^{+9.6}_{-10.6}$	0.132	13
Outer-8	68	43.4	39.2	3.9	0.4	$59.7^{+10.8}_{-11.7}$	0.072	50
Outer-9	66	20.2	17.0	3.0	0.2	$43.0^{+13.5}_{-15.3}$	0.044	80
Outer-10	81	31.8	28.0	3.6	0.2	$78.8^{+18.1}_{-20.0}$	0.028	96
Comb. K+L	1069	738.8	699.8	32.2	6.8	$55.6^{+2.6}_{-2.7}$	0.079	32

TABLE XII. Summary of the contributions to the systematic uncertainty in the measured neutrino capture rate.

Origin of uncertainty	Uncertainty (%)
Chemical Extraction Efficiency	
Efficiency of extraction from Ga metal, $\delta_{G1}$	$\pm 1.0$
Efficiency of synthesis into $\text{GeH}_4$ , $\delta_{G2}$	$\pm 1.3$
Carrier carryover, $\delta_{G3}$	negligible
Mass of Ga, $\delta_{G4}$	negligible
Chemical Extraction Subtotal	$\pm 1.6$
Counting Efficiency	
Calculated Efficiency	
Volume Efficiency, $\delta_{C1}$	-1.5, +1.8
Peak Efficiency, $\delta_{C2}$	$\pm 1.3$
Simulations to adjust for counter filling, Monte Carlo interpolation, $\delta_{C3}$	$\pm 0.6$
Calibration Statistics	
Gain Variation, $\delta_{C4}$	+0.4
Resolution, $\delta_{C5}$	$\pm 0.3$
Centroid, $\delta_{C6}$	$\pm 0.1$
Rise time cut, $\delta_{C7}$	negligible
Counting Efficiency Subtotal	-2.1, +2.3
Background Discrimination	
Residual Radon after Time Cuts, $\delta_{N1}$	-0.04
Solar Neutrino Background, $\delta_{N2}$	$\pm 0.20$
$^{71}\text{Ge}$ carryover, $\delta_{N3}$	$\pm 0.05$
Background Discrimination Subtotal	$\pm 0.2$
Total Systematic Uncertainty	-2.7, +2.9

### 1. Extraction Efficiencies

#### i. Extraction efficiency from Ga metal, $\delta_{G1}$

Special Ge carriers were produced with a known number of  $^{71}\text{Ge}$  contents [32]. These carriers were added to the reactors, and the numbers of  $^{71}\text{Ge}$  atoms extracted were counted and compared to the added numbers of  $^{71}\text{Ge}$  atoms. The ratio of extracted and added Ge atoms determines the extraction efficiency.

Two types of carrier with different enrichment in Ge isotopes  $^{72}\text{Ge}$  and  $^{76}\text{Ge}$  were used for the experiment. Both ligatures were made in 2015 and were used in preliminary solar measurements. Ge extraction efficiency was determined by a mass spectrometric method of extraction efficiency determination, which is based on isotopic measurements [38]. In this method, the efficiency of extraction of Ge from the Ga is calculated from the measured mass and isotopic content of added and extracted Ge and all relevant uncertainties (uncertainty in the total mass of Ge in the carrier, uncertainty in the Ge isotopic fractions of the carrier, uncertainty in the mass of Ge in the extracted sample, and uncertainty in the Ge isotopic fractions of the measured sample) are taken into account. The uncertainty of the extraction efficiency is  $\delta_{G1} = \pm 1.0\%$ .

#### ii. Efficiency of synthesis into $\text{GeH}_4$ , $\delta_{G2}$

An uncertainty in how much extracted carrier has been synthesized into  $\text{GeH}_4$ . The amount of germanium entering the counter is calculated from the volume of synthesized germane. The volume of germane is

determined using the calibrated stem of the Toepler pump, which is the main apparatus in the gas pumping system and the preparation of the working mixture of the counter. In the Toepler pump, there are two calibrated stems with measured volumes. Their volumes sizes were obtained by a large series of calibration measurements with uncertainty not higher than 1%. The calculation is based on the difference in mercury levels in the evacuated part of the Toepler pump, which is a manometric tube with a linear scale, and a calibrated stems of a precisely known volume, in which germane is located before being placed in the counter. Division value of the vertical scale of the pressure gauge tube is 1 mm, and the measurement error is half of 1 division, i.e. 0.5 mm. Measurement of the volume of germane is carried out in two calibrated volumes of the Toepler pump, that reduces the measurement error to  $\delta_{G2} = \pm 1.3\%$ .

#### iii. Carrier carryover, $\delta_{G3}$

The uncertainty of the amount of residual Ge carrier remaining from previous extractions  $\delta_{G3}$  with the mass spectrometric analysis, which is the part of the uncertainty in  $\delta_{G1}$ . Therefore, we assign negligible uncertainty to  $\delta_{G3}$ .

#### iv. Mass of Ga, $\delta_{G4}$

The gallium target mass affects the results of measurements of the neutrino capture rate indirectly via neutrino path length from a radioactive source through the gallium target in two zones. This uncertainty  $\delta_{G4}$  is taken

into account in determining the average neutrino path length in the gallium targets, which is given in Sec. V E.

## 2. Counting Efficiencies

Uncertainties associated with the counting efficiencies of pulses from  $^{71}\text{Ge}$  decays in proportional counters constitute the second group of uncertainties,  $\delta_C$ .

### i. Volume efficiency, $\delta_{C1}$

The volume efficiencies of the counters were measured at the end of the BEST measurements using two isotopes,  $^{37}\text{Ar}$  and  $^{71}\text{Ge}$ . Here, the volume efficiency is defined as the probability that the decay of a radioactive atom in the volume of a proportional counter would produce a detectable signal [32]. This efficiency was calculated for each detector by comparing the measured count rate in each count to the count rate in the high-efficiency standardization counter. A purified  $^{37}\text{Ar}$  gas was mixed with 90% Ar plus 10%  $\text{CH}_4$ , and the mixture is placed into counters under test. All counters were filled in turn with the same gas mixture. Three spectra were taken from each counter with each filling: the first with the voltage adjusted so that the  $^{37}\text{Ar}$  K peak is set at the middle of the scale to see all pulses with energies above the K peak, the second that both L and K peaks were on the scale, and the third with the L peak, whose energy is 270 eV, at about mid-scale. After the measurements, the mixture is transferred to the specially designed standardization counter with a volume efficiency of  $(99.5 \pm 0.6)\%$ , with a very high transfer efficiency  $E_{\text{transfer}} > 99.5\%$ . The standardization counter is brought to about the same pressure as in the test counter and the same spectra are measured. The ratio between the event rate above a certain threshold in the test counter,  $R_{\text{test}}$ , is then compared with the event rate above the same threshold in the standardization counter,  $R_{\text{test}}$ . After minor corrections, the volume efficiency of the counter is given by  $\epsilon_V = 0.995 R_{\text{test}} E_{\text{transfer}} D / R_{\text{standard}}$  where  $D$  is the decay factor of the  $^{37}\text{Ar}$  between the two measurements [32]. Additional measurements with  $^{71}\text{GeH}_4$  mixed with  $\text{Xe-GeH}_4$  were carried out using a similar technique described above for verification. The uncertainty assigned to volume efficiency is  $\delta_{C1} = +1.5 / -1.3\%$ . Considering that four counters were used twice in the BEST measurements this counting systematic uncertainty should be increased by 18%,  $\delta_{C1} = +1.8 / -1.5\%$ .

### ii. Counting efficiency in peaks, $\delta_{C2}$

The peak counting efficiency is the ratio of the number of registered pulses falling inside the  $\pm\text{FWHM}$  of the energy range of K and L peaks of  $^{71}\text{Ge}$  to the total number of counts. The value was determined by additional measurement using  $^{71}\text{Ge}$  for each counter. The details of the measurement are described in Appx. A. The average uncertainty for peak efficiencies was  $\delta_{C2} \pm 1.1\%$ .

Considering that four counters were used twice in the BEST measurements this counting systematic uncertainty should be increased by 18%,  $\delta_{C2} = \pm 1.3\%$ .

### iii. Monte Carlo Interpolation, $\delta_{C3}$

The counting efficiency is closely related to the pressure ( $P$ ) and the percentage ( $G$ ) of germane in the gas mixture [32]. The connection was obtained in measurements of volume efficiencies in a wide range of parameters for different counters. To obtain the counting efficiencies for arbitrary parameters of the gas mixture, Monte Carlo calculations are used. Varying the expression obtained in the analysis of measurements in accordance with the uncertainties of the pressure and the percentage of germane ( $\delta P = \delta G = 2\%$ ), we obtain  $\delta_{C3} = \pm 0.6\%$  for the K peak and  $\pm 0.4\%$  for the L peak.

### iv. Gain variation, $\delta_{C4}$

During long-term measurements, the gain of the counting system may drift resulting in uncertainty in energy determination. The drifts in the positions of the  $^{55}\text{Fe}$  calibration peak were measured during the first month of each counting. The average percentage of deviation from the mean values was  $\pm 1.1\%$ . To measure the uncertainty due to the energy determination, the calibration peak positions were shifted by  $\pm 1.1\%$  and the capture rates in the inner and the outer targets were obtained. This variation study yielded the gain variation uncertainty of  $\delta_{C4} = +0.4\%$ . This uncertainty is one-sided because the gain drift can only reduce the number of selected events.

### v. Resolution and centroid, $\delta_{C5}$ and $\delta_{C6}$

The systematic uncertainty of the energy resolution of the calibrations was determined similarly to item iv. The average percentage of deviation of the resolution of the calibration peaks in the first month of measurements was  $\pm 2\%$ , which gives the value  $\delta_{C5} = \pm 0.3\%$ . Similarly, the deviation of the centroid of the calibration peaks gives the value  $\delta_{C6} = \pm 0.1\%$ .

### vi. Rise time cut, $\delta_{C7}$

At the end of the measurement, an additional study using  $^{71}\text{Ge}$  was carried out to determine the rise time ( $T_N$ ) values of pulses inside the 2 FWHM regions of the L and K peaks of  $^{71}\text{Ge}$ . Therefore, in contrast to the previous SAGE experiments where the average  $T_N$  limits were used [32], there is no uncertainty associated with the incorrect determination of the  $T_N$  limit interval. Hence, we assign negligible uncertainty to  $\delta_{C7}$ .

## 3. Background Discrimination

Uncertainties arising from background discrimination constitute the third group of uncertainties,  $\delta_N$ .

### i. Residual radon after the time cuts, $\delta_{N1}$

The number of false  $^{71}\text{Ge}$  events due to internal  $^{222}\text{Rn}$  is equal to the number of detected saturated pulses induced by Rn decay ( $N_{\text{Rn}}$ ) multiplied by the survival probability of false events after the event selection  $\alpha_{K+L}$  [32]. The fraction of the false events to the total number of events  $N$  in K and L peaks is treated as a systematic uncertainty

$$\begin{aligned}\delta_{N1} &= \frac{N_{\text{Rn}} \times \alpha_{K+L}}{N} \\ &= \frac{425.9 \times (4.3 + 7.8) \times 10^{-4}}{738.8 + 724.0} \\ &= 0.035\% .\end{aligned}\quad (16)$$

This uncertainty is one-sided negative because the effect of the residual Rn is a reduction in the detected number of events.

**ii. Solar neutrinos,  $\delta_{N2}$**  Solar neutrinos are the largest source of background in the BEST experiment. They interact with the Ga targets at a constant rate, and this background is taken into account in the analysis of each measurement. During solar neutrino measurements, the number of solar-neutrino-induced events in the inner and outer target zones was obtained to be 6.1 (see Table X) and 32.2 (see Table XI). These values are compared with the total number of pulses recorded in K and L peaks - 724.0 and 738.8. The solar neutrino flux and thus the uncertainty associated with it are obtained from previous gallium solar measurements as  $(66.1 \pm 3.1)$  SNU [32], the uncertainties are calculated to be  $\delta_{N2} = 6.1/724.0 \times 3.1/66.1 = 0.04\%$  for the inner zone and  $\delta_{N2} = 32.2/738.8 \times 3.1/66.1 = 0.2\%$  for the outer zone.

**iii.  $^{71}\text{Ge}$  carryover,  $\delta_{N3}$**

The uncertainty associated with the  $^{71}\text{Ge}$  remaining after extractions is found as the product of the statistical uncertainty and the ratio of the carryover events ( $N_{CO}$ ) to the total number of recorded events ( $N$ )

$$\delta_{N3} = \frac{N_{CO}}{N} \times \delta_N , \quad (17)$$

where  $\delta_N = 1/\sqrt{N}$  [32]. We obtain 0.03% and 0.05% uncertainties for the inner and the outer zones.

#### 4. Average Path Length Uncertainty

The mass of the internal target obtained from the considered geometry is 63.1 kg more gallium than compared with the mass measurement. Such a difference in the target gallium mass will have the maximum effect on the change in the path length if we assume a change in the inner radius of the sphere by 0.18 cm. We take the resulting change in the radius as the radius uncertainty,

which leads to a systematic uncertainty in the neutrino path length in the inner target of 0.3%. For the external target, the corresponding uncertainty is 0.

The outer radius of the spherical vessel was measured in a direct way, with a ruler, when the sphere vessel was available for measurements in the underground laboratory of the GGNT. The surface of the sphere was covered with a layer of epoxy resin. The maximum irregularities of the coating did not exceed 1 mm, which varies the average neutrino path length in the outer target of the cylindrical zone by 0.2%. Variations in the internal dimensions of the cylindrical zone, as well as possible inaccuracies in the relative position of the axes of the two zones of the target do not exceed 1 mm. A change in the dimensions of the cylindrical zone within the indicated values leads to a change in the average neutrino path length by approximately the same 0.18 cm. Therefore, we take the total uncertainty of the average neutrino path length in the cylindrical zone to be 0.3%, *i.e.*, the uncertainties of the average neutrino path length in both target zones are assumed to be equal.

The total systematic uncertainty, added in quadrature, is  $-2.7/+2.9\%$ . Including both the statistical and systematic uncertainties, we obtain  $^{71}\text{Ge}$  production rates of

$$\begin{aligned}r_{\text{In-meas.}} &= [54.9 \pm 2.5(\text{stat.})_{-1.5}^{+1.6}(\text{syst.})] \text{ atoms/d} \\ &= [54.9_{-2.9}^{+3.0}] \text{ atoms/d} , \\ r_{\text{Out-meas.}} &= [55.6 \pm 2.7(\text{stat.})_{-1.5}^{+1.6}(\text{syst.})] \text{ atoms/d} \\ &= [55.6_{-3.1}^{+3.1}] \text{ atoms/d} .\end{aligned}\quad (18)$$

Various efficiencies for individual extraction are collected and summarized in Table XIII. The fractional uncertainties are the same for every extractions and given in Table XII. The saturation factor in the table represents the saturation in production rate due to  $^{71}\text{Ge}$  and  $^{51}\text{Cr}$  activities and is given by

$$\begin{aligned}f_s &= \exp(-\lambda_{51}(t_s - T)) \\ &\times [\exp(-\lambda_{51}\theta_{\text{Cr}}) - \exp(-\lambda_{71}\theta_{\text{Cr}})] / (1 - \lambda_{51}/\lambda_{71}) ,\end{aligned}\quad (19)$$

where  $\lambda_{51}$  and  $\lambda_{71}$  are the decay constants of  $^{51}\text{Cr}$  and  $^{71}\text{Ge}$ ,  $t_s$  is the start time of each source exposure,  $T$  is the source activity reference time and  $\theta_{\text{Cr}}$  is the time of exposure of the Ga to the  $^{51}\text{Cr}$  source [24]<sup>2</sup>. All parameters considered in the calculation of  $f_s$  are very well established, and therefore its uncertainty is negligible. The

<sup>2</sup> One should note that there is a typographical error in Eq. 4 of Ref. [24]. There is a missing division sign in the denominator, which is corrected in Eq. 19 here in this work. The correct denominator is  $(1 - \lambda_{51}/\lambda_{71})$ .

TABLE XIII. Summary of BEST detection efficiencies. The extraction efficiency values are taken from Tables I and II. The counter efficiency values and  $\Delta$  are taken from Tables III and IV. Same fractional uncertainties listed in Table XII are assigned to each extraction. The saturation factor is obtained from Eq. 19 with negligible uncertainty.

Extraction	Extraction efficiency (into GeH <sub>4</sub> )	Saturation factor	Counter efficiency (K peak)	$\Delta_K$	Total detection efficiency (K peak)	Counter efficiency (L peak)	$\Delta_L$	Total detection efficiency (L peak)
Inner-1	0.946	0.3924	0.3663	0.8100	0.1101	0.3803	0.7450	0.1052
Inner-2	0.9559	0.3731	0.3647	0.7839	0.1020	0.3785	0.6542	0.0883
Inner-3	0.9673	0.3752	0.3605	0.7143	0.0935	0.3599	0.7143	0.0933
Inner-4	0.9515	0.3750	0.3679	0.7870	0.1033	0.3769	0.3669	0.0493
Inner-5	0.9554	0.3779	0.3649	0.7470	0.0984	0.3654	0.7470	0.0986
Inner-6	0.9548	0.3735	0.3577	0.7714	0.0984	0.3604	0.3891	0.0500
Inner-7	0.9381	0.3760	0.3676	0.7495	0.0972	0.3793	0.6739	0.0902
Inner-8	0.9789	0.3761	0.3656	0.7754	0.1044	0.3779	0.7865	0.1094
Inner-9	0.9545	0.3761	0.359	0.8015	0.1033	0.361	0.8015	0.1039
Inner-10	0.9372	0.3770	0.3698	0.7629	0.0997	0.3755	0.8002	0.1062
Outer-1	0.9503	0.3924	0.3422	0.7646	0.0976	0.3596	0.6996	0.0938
Outer-2	0.9581	0.3731	0.3707	0.8043	0.1066	0.3792	0.6755	0.0916
Outer-3	0.9668	0.3752	0.2933	0.7650	0.0814	0.3358	0.7650	0.0932
Outer-4	0.9622	0.3750	0.3658	0.7819	0.1032	0.381	0.3755	0.0516
Outer-5	0.9609	0.3779	0.3568	0.8025	0.1040	0.3727	0.8025	0.1086
Outer-6	0.9253	0.3735	0.3585	0.8009	0.0992	0.3577	0.3845	0.0475
Outer-7	0.9514	0.3760	0.3407	0.7976	0.0972	0.3607	0.7107	0.0917
Outer-8	0.9897	0.3761	0.3716	0.8295	0.1147	0.3785	0.8406	0.1184
Outer-9	0.9664	0.3761	0.293	0.7865	0.0838	0.336	0.7865	0.0961
Outer-10	0.9538	0.3770	0.3677	0.7567	0.1001	0.3797	0.7940	0.1084

total efficiency is the product of the chemical extraction efficiency, the saturation factor, and the counting efficiency [24]. The typical value of the total efficiency is  $(10.0 \pm 0.3\%)$ , where systematic uncertainties are included.

Fig. 9 shows the K+L production rate fits for the inner and the outer zones. The upper panel for each zone shows the production rate at the start of each exposure, and the lower panel shows the rate normalized to the reference time. The results are plotted at the start of each exposure where the production rates are fit to. The vertical lines represent the uncertainty of the fits, while horizontal lines only define the exposure period. The ratio of measured to predicted production rates are

$$R_{\text{In}} = \frac{54.9_{-2.9}^{+3.0}}{69.4_{-2.0}^{+2.5}} = 0.79_{-0.05}^{+0.05}, \quad (20)$$

$$R_{\text{Out}} = \frac{55.6_{-3.1}^{+3.1}}{72.6_{-2.1}^{+2.6}} = 0.77_{-0.05}^{+0.05}.$$

These are  $4.2 \sigma$  and  $4.8 \sigma$  less than unity, respectively. As a cross-check, the  $^{51}\text{Cr}$  half-life was left free and fitted to the data. The values of half-life from fits to the inner and the outer targets were  $(30.97 \pm 3.90)$  d and  $(31.55 \pm 2.89)$  d. They agree with the known  $^{51}\text{Cr}$  half-life of  $(27.704 \pm 0.004)$  [35].

The ratio between the inner and the outer zones  $R_{\text{out}}/R_{\text{in}} = (0.77 \pm 0.05)/(0.79 \pm 0.05) = 0.97 \pm 0.08$  is unity within uncertainty, and hence there is no difference in the capture rates between the two zones.

## H. Oscillation Analysis

For  $n = 1, \dots, N$  experiments (the two BEST volumes are treated separately), oscillation parameters are estimated by a global minimization of

$$\chi^2(\Delta m^2, \sin^2 2\theta) = (\mathbf{r}^{\text{meas.}} - \mathbf{r}^{\text{calc.}})^T \mathbf{V}^{-1} (\mathbf{r}^{\text{meas.}} - \mathbf{r}^{\text{calc.}}), \quad (21)$$

where  $\mathbf{r}^{\text{meas.}}$  ( $\mathbf{r}^{\text{calc.}}$ ) is the vector of the measured (calculated) rates with  $r_i^{\text{calc.}}(\Delta m^2, \sin^2 2\theta)$  and  $V$  is the covariance matrix with

$$V_{nk} = \delta_{nk} \varepsilon_n^2 + \varepsilon_{CS}^n \times \varepsilon_{CS}^k, \quad (22)$$

where  $\varepsilon_n^2 = \varepsilon_{n,\text{stat}}^2 + \varepsilon_{n,\text{sys}}^2$  are uncorrelated uncertainties comprised of statistical and systematic measurement uncertainties, and  $\varepsilon_{CS}^n$  represent the correlated uncertainties of  $\sigma$  [57]. For Ga source experiments, the cross-section uncertainties are the only significant contribution to the correlated uncertainty. The uncertainties of the Bahcall cross-section for measurements with a chromium source are equal to  $+3.6/-2.8\%$ , and hence we use  $\pm 3.6\%$  for the calculation. In the measurement with an argon source, the cross-section uncertainties do not change the values of the shown uncertainty due to their relative smallness.

Fig. 10 illustrates the exclusion contours corresponding to  $1\sigma, 2\sigma$ , and  $3\sigma$  confidence levels with the two BEST results assuming the correlated cross section uncertainties. The best-fit result is at  $\sin^2 2\theta = 0.42_{-0.17}^{+0.15}$ ,  $\Delta m^2 = 3.3_{-2.3}^{+\infty}$  eV<sup>2</sup>, and the contours refer to  $\chi^2 = \chi_{\text{min}}^2 + \Delta\chi^2$  for which  $\Delta\chi^2 = 2.30, 6.18, 11.83$  with two degrees of

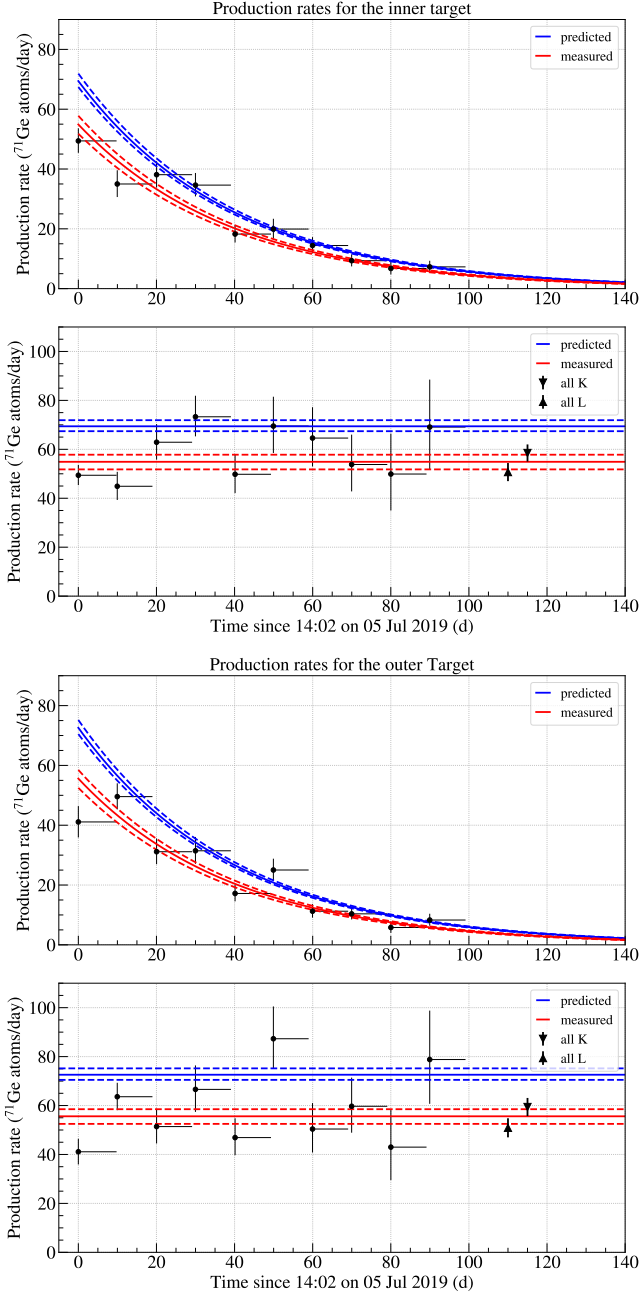


FIG. 9. **Top:** the measured K+L peak rates of the inner target volume. **Middle-top:** the production rates of the inner target volume normalized to the reference time. The combined results for events in the L and K peaks are shown separately and compared to the predicted rate. **Middle-bottom:** the measured K+L peak rates of the outer target volume. **Bottom:** the production rates of the outer target volume normalized to the reference time. The combined results for events in the L and K peaks are shown separately and compared to the predicted rate. The blue (red) region represents the predicted (measured) production rate. The dotted lines enclose the  $\pm 1\sigma$  uncertainty regions.

freedom have the coverage probability of 68.27% ( $1\sigma$ ),

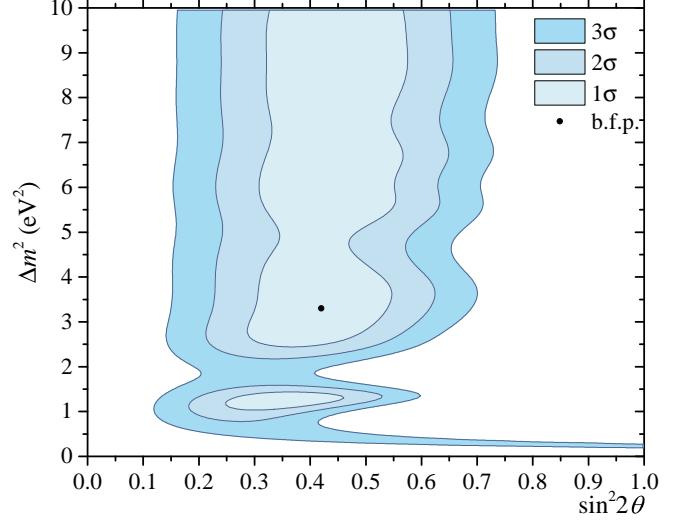


FIG. 10. Allowed regions for two BEST results. The best-fit point is  $\sin^2 2\theta = 0.42^{+0.15}_{-0.17}$ ,  $\Delta m^2 = 3.3^{+\infty}_{-2.3}$  eV<sup>2</sup> and is indicated by a point.

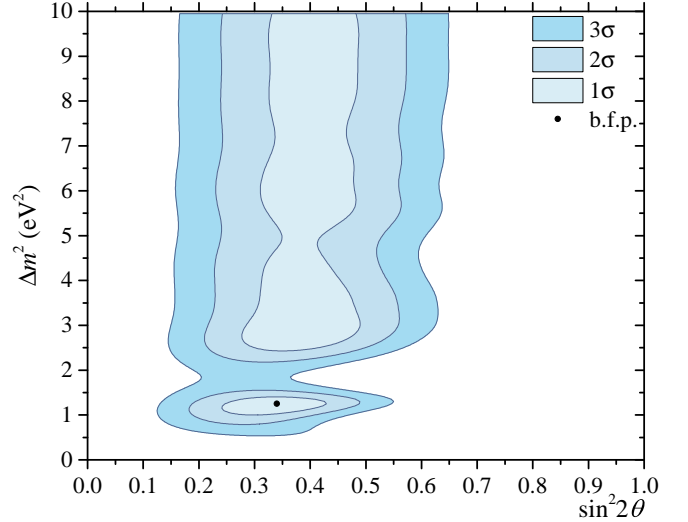


FIG. 11. Allowed regions for two GALLEX, two SAGE and two BEST results. The best-fit point is  $\sin^2 2\theta = 0.34^{+0.14}_{-0.09}$ ,  $\Delta m^2 = 1.25^{+\infty}_{-0.25}$  eV<sup>2</sup> and is indicated by a point.

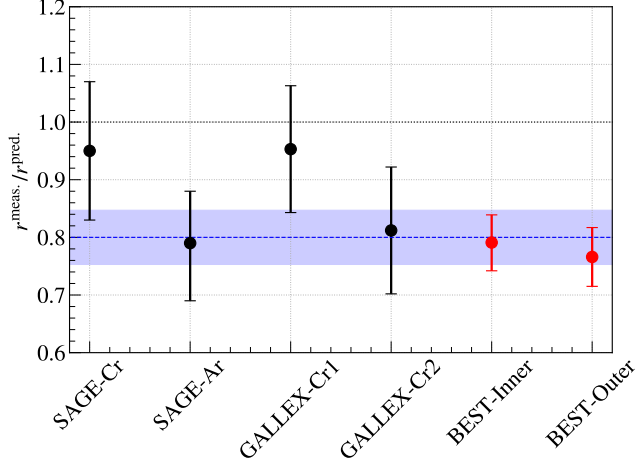
95.45% ( $2\sigma$ ) and 99.73% ( $3\sigma$ ), respectively [58]. This approximation is based on Wilks' theorem. A concern about the applicability of Wilks' theorem in the oscillation analysis [59] was investigated and found to have a small effect on the analysis [60].

We also combine the BEST results with the previous SAGE and GALLEX source experiments to plot combined exclusion plots. Table XIV and Fig. 12 summarize results from all gallium anomaly experiments, including the SAGE [24, 25] and the GALLEX results [27].

If the cross-section uncertainties are considered to be completely uncorrelated to each other and to the other uncertainties, they can be added in quadrature as

TABLE XIV. Results of all six Ga source experiments.

Experiment	$R$
SAGE-Cr [24]	$0.95 \pm 0.12$
SAGE-Ar [25]	$0.79 \pm 0.095 (+0.09 / -0.10)$
GALLEX-Cr1 [27]	$0.953 \pm 0.11$
GALLEX-Cr2 [27]	$0.812 \pm 0.11$
BEST-Inner	$0.791 \pm 0.05$
BEST-Outer	$0.766 \pm 0.05$

FIG. 12. Ratios of measured and predicted  $^{71}\text{Ge}$  production rates in all Ga source experiments. The combined result is shown as a blue band.

$$\sigma_i = \sqrt{\sigma_{i,\text{others}}^2 + (0.032 \times R_i)^2}, \quad (23)$$

and the combined result  $R_0$  is obtained by the sum  $R_0 = \sum_i (w_i \cdot R_i)$ , where  $w_i = (\sigma_0 / \sigma_i)^2$  and  $\sigma_0 = 1 / \sqrt{\sum_i (1 / \sigma_i^2)}$ . The result is given as  $R_0 \pm \sigma_0 = 0.81 \pm 0.03$ . The total uncertainty is 4.0%.

If we consider the correlation between systematic uncertainties, the average value of  $R_{0,\text{Cr}}$  is obtained first, and then combined with the SAGE-Ar experiment afterward. The uncertainty from the cross section evaluation is the only significant contribution to the correlated uncertainty, and hence the combined result of all six gallium anomaly experiments is given as

$$R_0 = \left(\frac{\sigma_R}{\sigma_{\text{Cr}}}\right)^2 \cdot R_{\text{Cr}} + \left(\frac{\sigma_R}{\sigma_{\text{Ar}}}\right)^2 \cdot R_{\text{Ar}} \pm \sigma_R, \quad (24)$$

where  $\sigma_R = 1 / \sqrt{(1 / \sigma_{\text{Cr}}^2 + 1 / \sigma_{\text{Ar}}^2)}$ ,  $R_{\text{Cr}} = \sum_i^{\text{Cr}} (w_i \cdot R_i)$ ,  $w_i = (\sigma_0 / \sigma_{i,\text{others}})^2$ ,  $\sigma_0 = 1 / \sqrt{\sum_i^{\text{Cr}} (1 / \sigma_{i,\text{others}}^2)}$  and  $\sigma_{\text{Cr}} = \sigma_0 + 0.032 \cdot R_{\text{Cr}}$ , with the uncertainty of the total Cr measurements is obtained by summing over. The combined result of all six measurements is obtained as  $R_0 = 0.80 \pm 0.047$ . The total uncertainty is 6.1%, which is larger than the uncorrelated estimation. The result is illustrated in Fig. 12 as a blue band.

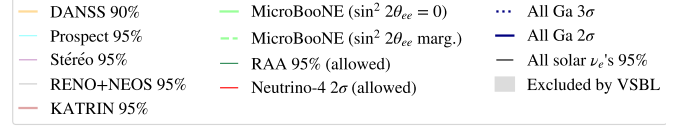


FIG. 13. Exclusion contours of all gallium anomaly experiments: two GALLEX, two SAGE and two BEST results. The blue solid line and the blue dotted line show the  $2\sigma$  and  $3\sigma$  confidence level, respectively. The figure also presents the exclusion contours from Prospect [61], DANSS [62], Stéréo [63], KATRIN [64], the combined analysis of RENO and NEOS data [65], reactor anti-neutrino anomalies (RAA) [22], interpretations of the MicroBooNE result for the oscillation hypothesis with fixed mixing angle ( $\sin^2 2\theta$ ) and profiled over the angle [30], and the model-independent 95% upper bound on  $\sin^2 2\theta$  from all solar neutrino experiments [66]. The  $2\sigma$  allowed region of Neutrino-4 [67] is also presented and the grey shading represents the merged exclusion of the very short baseline (VSBL) null results.

Fig. 11 presents the combined result from all gallium source experiments; SAGE, GALLEX and BEST, considering the correlated cross section uncertainties. The best-fit result from the combined analysis of all Ga source experiments is  $\sin^2 2\theta = 0.34_{-0.09}^{+0.14}$ ,  $\Delta m^2 = 1.25_{-0.25}^{+0.28}$  eV $^2$ .

Fig. 13 compares the combined result from all gallium anomaly experiments to some other sterile neutrino search experiments. The exclusion curves of Prospect [61], DANSS [62], Stéréo [63], KATRIN [64], the combined analysis of RENO and NEOS data [65]. One can see that the gallium anomaly result is still in a strong tension with these experiments except a tiny region above 8 eV $^2$ . The interpretations of the MicroBooNE result for the oscillation hypothesis either fixed or profiled over the mixing angle ( $\sin^2 2\theta$ ) [30] are also presented. These results do not either favor or exclude the allowed region for the gallium anomaly experiments. The 95% allowed region from the reactor antineutrino anomalies (RAA) [22] is also illustrated in the figure. One can see that the tension between the Ga anomalies and the RAA still persists. The figure also shows the  $2\sigma$  allowed

region of Neutrino-4 [67] and the model-independent 95% solar neutrino upper bound on  $\sin^2 2\theta$  [66]. The Neutrino-4 allowed region is within the  $3\sigma$  bound, and therefore is not excluded by the gallium anomaly experiments. The model-independent 95% solar neutrino bound on  $\sin^2 2\theta$  excludes most of the  $2\sigma$  allowed region, but the parameter space near  $\Delta m^2 \approx 1 \text{ eV}^2$  is not entirely excluded.

## VI. DISCUSSION

The deficits in the production rates observed in both volumes are consistent with the results from previous gallium source experiments, confirming the gallium anomaly. While no difference in the production rates in the two target zones is observed and the oscillation length cannot be well constrained, the large deviation of  $R$ 's from unity indicates that the oscillation hypothesis is favored over no-oscillation hypothesis to the extent of current knowledge. Effects from systematic errors in the extraction efficiency, the counting efficiency, Ga target mass, the geometry of the system, the source strength and the counting system operation have been thoroughly considered and confirmed by additional measurements to be small (see Tables IX and XII) compared to the observed deficits. In addition, GALLEX's  $^{71}\text{As}$  experiment [68] ruled out any chemical effects of 'hot atoms' that would make it difficult to extract  $^{71}\text{Ge}$  atoms formed during neutrino capture. Since the physics processes involved in the Ga experiments are simple and understood very well, it is hard to attribute the result to some unaccounted effects. The  $^{71}\text{Ge}$  decay rate is very well known, and the neutrino-nucleon cross-section  $\sigma$  to the ground state in  $^{71}\text{Ga}$  is hence also well determined. The  $\sigma$  cannot be reduced below the ground state value by considering the excited state contribution to be zero. The transition to excited states cannot decrease the overall value of the total  $\sigma$  and hence cannot be the origin of the reported deficits. When the solar neutrino flux measured by the SAGE [41] is compared to the Borexino [69] result, the two experiments claim similar  $pp$  flux. SAGE measured the  $pp$  flux produced in the Sun to be  $(6.0 \pm 0.84) \times 10^{10} / (\text{cm}^2 \text{ s})$ , while Borexino yielded  $6.1 \pm 0.05_{-0.5}^{+0.3} \times 10^{10} / (\text{cm}^2 \text{ s})$ . However, the uncertainties are too large to either confirm or exclude the overall efficiency as explanation of the gallium anomaly. Other explanations without sterile neutrinos are possible but would inevitably require some fundamental misunderstanding of nuclear or atomic physics.

After the BEST measurements the gallium anomaly is more significant; the weighted average value of the neutrino capture rate relative to the expected value for all Ga experiments is  $0.80 \pm 0.05$ . The result indicates that the oscillation length is similar to, or smaller than, the volume of the BEST targets. Hence,  $\Delta m^2$  is unbounded from above by the BEST experiment. A future Ga experiment with shorter baseline would help constraining the value of  $\Delta m^2$ , but it would require the use of stronger

neutrino source which would be challenging. The use of neutrino source with larger neutrino energy could also be considered.

## VII. CONCLUSION

The first result from the BEST sterile neutrino oscillation experiment was presented. We report 21% and 23% deficits of the  $^{71}\text{Ge}$  production rates based on the cross section [45] in the inner and the outer zones of the BEST Ga target. The values are consistent with the previously reported gallium anomaly from SAGE and GALLEX experiments, with higher significance. The weighted average value of the neutrino capture rate relative to the expected value for all Ga experiments is  $0.80 \pm 0.05$ , which corresponds to a  $4\sigma$  deviation from unity. If attributed to the neutrino oscillation to sterile state, the result corresponds to the best fit of  $\Delta m^2 = 3.3_{-2.3}^{+\infty} \text{ eV}^2$  and  $\sin^2 2\theta = 0.42_{-0.17}^{+0.15}$ . No difference in the capture rates from the two zones at different distances is observed. This indicates a neutrino oscillation at a scale shorter than the BEST dimensions.

The allowed region in the  $(\Delta m^2, \sin^2 2\theta)$  parameter space for all combined Ga source experiments shows that the Ga anomalies are still in tension with most other sterile neutrino search experiments. On the other hand, the Neutrino-4 allowed region coincides with the gallium anomaly result, and therefore is not rejected by the Ga source experiments. The value of  $\Delta m^2$  should be better constrained to conclusively determine whether the Neutrino-4 result is accepted or rejected by the Ga source experiments.

Ga source experiments are unique in their capability of searching for the very short range neutrino oscillation at a meter scale, and the simplicity of the physics involved. They can provide critical information on the field of the sterile neutrino search experiments, providing a key to detect the neutrino oscillation to sterile states and the opportunity of resolving the existing tension between the reactor antineutrino experiments and other experiments. Further study with other neutrino sources will enhance our knowledge on the gallium anomaly, and hence lead to an irreplaceable contribution to the pursuit of the physics beyond the Standard Model.

## ACKNOWLEDGMENTS

We thank V. A. Rubakov for constant stimulation of our interest and for fruitful discussions. This work is supported by Federal Agency for Scientific Organizations (FANO), Ministry of Education and Science of Russian Federation under agreement no. 14.619.21.0009 (unique project identifier no. RFMEFI61917X0009), State Atomic Energy Corporation Rosatom, and the Office of Nuclear Physics of the US Department of Energy.

TABLE XV. A summary of the  $^{71}\text{Ge}$  counter calibration.

Counter	$^{55}\text{Fe}$			L-peak						K-peak							
	Pos. (a.u.)	Resol. (%)	En non-linearity factor	Position			Resolution			Position			Resolution				
				Pred. from $^{55}\text{Fe}$ (a.u.)	True (a.u.)	Ratio	Pred. from $^{55}\text{Fe}$ (%)	True (%)	Ratio	Pred. from $^{55}\text{Fe}$ (a.u.)	True (a.u.)	Ratio	Pred. from $^{55}\text{Fe}$ (%)	True (%)	Ratio		
<b>sys2z</b>																	
YCN43	437.39	18.2	0.982	86.81	87.16	1.00	40.92	40.29	0.98	755.35	725.50	0.96	15.88	12.98	0.82		
YCNA9	431.86	19.7	0.938	85.71	86.32	1.01	44.29	42.57	0.96	712.39	728.84	1.02	17.19	16.02	0.93		
YCN41	442.80	18.0	0.967	87.88	87.00	0.99	40.40	37.24	0.92	753.01	732.49	0.97	15.68	13.34	0.85		
YCN46	448.93	18.5	0.915	89.10	90.61	1.02	41.48	39.62	1.04	722.39	748.55	0.96	16.10	14.16	0.88		
Mean sys2z						1.00			0.96			1.00			0.87		
std						0.01			0.03			0.04			0.05		
<b>sys3</b>																	
YCN113	337.36	18.8	0.982	66.96	57.71	0.86	42.09	42.13	1.00	582.61	564.38	0.97	16.34	14.13	0.86		
YCT92	334.67	18.9	0.964	66.42	56.72	0.85	42.40	41.88	0.99	567.37	563.97	0.99	16.46	13.90	0.84		
YCT3	342.65	19.3	0.932	68.01	58.24	0.86	43.23	40.61	0.94	561.61	576.97	1.03	16.78	14.19	0.85		
YCT2	337.00	18.8	0.982	66.89	57.77	0.86	42.24	41.62	0.99	581.98	563.33	0.97	16.40	14.05	0.86		
YCT9	334.80	19.1	0.978	66.45	57.97	0.87	42.90	39.42	0.92	575.83	569.62	0.99	16.65	13.89	0.83		
YCT97	332.81	18.6	0.932	66.05	57.11	0.86	41.64	38.75	0.93	545.48	559.25	1.03	16.16	13.51	0.84		
Mean sys3						0.86			0.96			1.00			0.85		
std						0.01			0.03			0.03			0.01		

TABLE XVI. A summary of the  $T_N$  event selection efficiency test using  $^{71}\text{Ge}$  calibration data.

Counter	Num. Ev. L- all	L-peak $T_N$ cut (ns)	Num. Ev L- selected	ratio	Num. Ev. k- all	K-peak $T_N$ cut (ns)	Num. Ev k- selected	ratio
<b>sys2z</b>								
YCN43	495	10	463	0.94	489	13.2	468	0.96
YCNA9	1281	13.2	1244	0.97	1167	18.8	1142	0.98
YCN41	1353	10.3	1299	0.96	1434	13.4	1374	0.96
YCN46	941	11.3	897	0.95	865	15.2	837	0.97
mean 2z				0.95				0.97
std				0.01				0.01
<b>sys3</b>								
YCN113	1643	9.1	1626	0.99	1488	13.6	1426	0.96
YCT92	265	13.0	250	0.94	243	17.6	237	0.98
YCT4	508	10.2	497	0.98	328	13.2	313	0.95
YCT3	314	10.3	297	0.95	258	16.4	252	0.98
YCT2	1475	10.1	1415	0.96	1483	16.6	1427	0.96
YCT9	397	9.1	388	0.98	341	14.9	322	0.94
YCT97	1622	11.4	1551	0.96	1607	17.3	1562	0.97
mean sys3				0.96				0.96
std				0.02				0.02

## Appendix A: $^{71}\text{Ge}$ Calibration

### 1. Correction for Energy Calibration

To verify the extrapolation for the K and L peak regions from the  $^{55}\text{Fe}$  calibration peak, counters were filled with  $^{71}\text{Ge}$  for additional analysis. Positions and resolutions of the peaks from extrapolation were compared to the true  $^{71}\text{Ge}$  peaks. This analysis also enables to select events with real  $T_N$  limits and verify the accepted value of 96% acceptance.

Table XV summarizes the positions and the resolutions of the  $^{55}\text{Fe}$  calibration and the  $^{71}\text{Ge}$  K and L peaks. The values predicted from the calibration peak, taking into

account the counter non-linearity factors, are presented with the true location of the X-ray peaks. Means and standard deviations of the two types of counter systems: sys2z (new) and sys3 (old), are also presented for each peak. These values are used as correction factors for the event selection.

### 2. Rise time window $T_N$ Selection Test

The  $^{71}\text{Ge}$  calibration data is also used as a test to the  $T_N$  limits event selection windows. The cutoff values, determined as the ratio of  $T_N$  selected events to all events without selection, is expected to be close to 96%. The values presented in Table XVI agrees with 96% within

TABLE XVII. BEST results without the first Cr extractions

Extraction	Number of candidate events	Number fit to $^{71}\text{Ge}$	Number of events assigned to				$Nw^2$	Probability (%)
			$^{51}\text{Cr}$ source production	Solar $\nu$ production	Carryover	$^{71}\text{Ge}$ Production decay rate (atoms/day)		
Inner 9 Ex.	913	553.9	538.9	5.3	9.7	$57.7^{+3.2}_{-3.1}$	0.093	26
Outer 9 Ex.	889	599.7	564.5	28.5	6.6	$59.8^{+3.1}_{-3.2}$	0.058	59

uncertainty. Hence the  $T_N$  event selection efficiency is verified.

### Appendix B: Results without the First Data Points

In Fig. 9, it seems that the most significant contributions to the deficit for both the inner and the outer volumes originate from the first extractions. To examine the effect of the first extraction, we carried out an analysis leaving out the first extraction. For the 9 runs of each target without the first extractions, the combined best fit rates are:

$$\begin{aligned} r_{\text{In-meas.}} &= 57.7 \pm 3.2 \text{ atoms}^{71}\text{Ge/day} , \\ r_{\text{Out-meas.}} &= 59.8 \pm 3.2 \text{ atoms}^{71}\text{Ge/day} . \end{aligned} \quad (\text{B1})$$

These are 3% and 6% increase in rates, respectively. The statistical uncertainty with 68% confidence increases by 19% in the two volumes. The quadratic combination of all systematic uncertainties is  $-2.7/+2.9\%$ . The values are summarized in Table XVII.

The measured production rates in the K and L peaks, including both statistical and systematic uncertainties combined in quadrature are

$$\begin{aligned} r_{\text{In-meas.}} &= 57.7 \pm 3.2(\text{stat.})^{+1.7}_{-1.6}(\text{syst.}) \\ &= 57.7^{+3.6}_{-3.6} \text{ atoms}^{71}\text{Ge/day} , \\ r_{\text{Out-meas.}} &= 59.8 \pm 3.2(\text{stat.})^{+1.7}_{-1.6}(\text{syst.}) \\ &= 59.8^{+3.6}_{-3.6} \text{ atoms}^{71}\text{Ge/day} . \end{aligned} \quad (\text{B2})$$

The ratio of measured to predicted production rates are

$$\begin{aligned} R_{\text{In}} &= \frac{57.7^{+3.6}_{-3.6}}{69.4^{+2.5}_{-2.0}} = 0.83^{+0.06}_{-0.06} , \\ R_{\text{Out}} &= \frac{59.8^{+3.6}_{-3.6}}{72.6^{+2.6}_{-2.1}} = 0.82^{+0.06}_{-0.06} . \end{aligned} \quad (\text{B3})$$

These are  $2.9\sigma$  and  $3.1\sigma$  less than unity. The ratio of the outer to the inner result is  $0.99 \pm 0.08$  and there is no difference in the capture rates in the two zones. In Fig. 14, the allowed region for the BEST result and for all gallium anomaly experiments are illustrated.

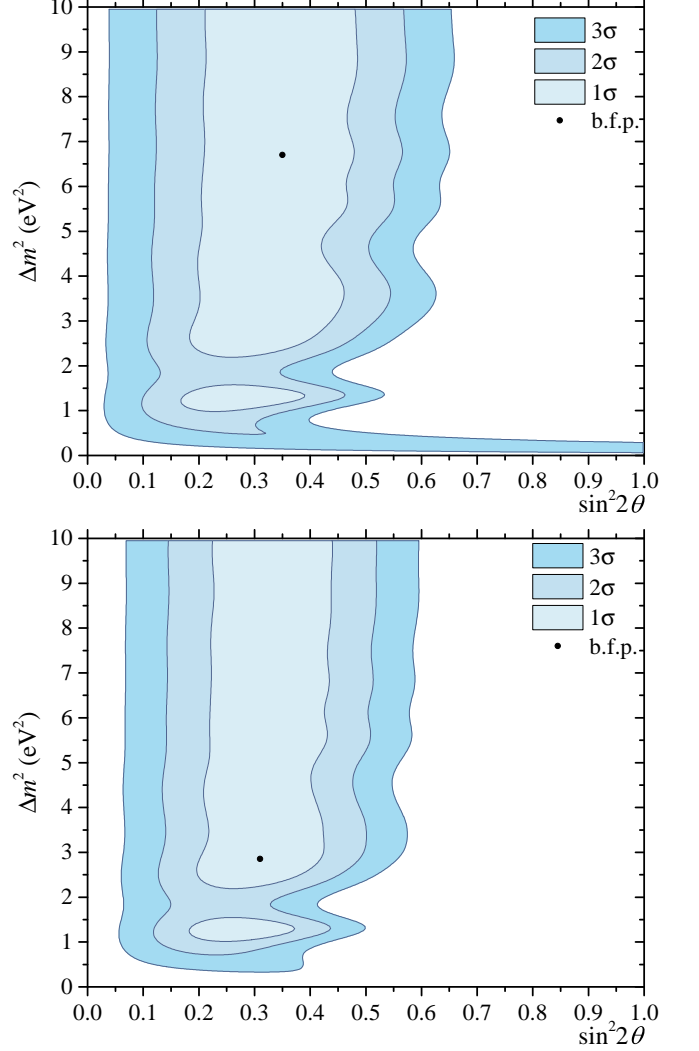


FIG. 14. **Top:** Allowed regions for two BEST results without the first extractions. The best-fit point is  $\sin^2 2\theta=0.35$ ,  $\Delta m^2 = 6.7 \text{ eV}^2$  and is indicated by a point. **Bottom:** Allowed regions for two GALLEX, two SAGE and two BEST results without the first extractions. The best-fit point is  $\sin^2 2\theta=0.31$ ,  $\Delta m^2 = 2.85 \text{ eV}^2$  and is indicated by a point.

### Appendix C: $^{51}\text{Cr}$ Branching Ratio Uncertainty

The calorimetric heat measurement relies on the branching ratio of the 320 keV  $^{51}\text{Cr}$  emission to normalize to activity. If the branching value is in error, so would

be the source strength.

TABLE XVIII. A summary of the branching ratio of the 320 keV emission from  $^{51}\text{Cr}$ .

Branching ratio	Reference	Method
0.1030(19)	[70]	Ge(Li)
0.0990(8)	[71]	NaI
0.1008(11)	[71]	HPGe
0.099(1)	[72]	HPGe (Beta-gamma coincidence)
0.0987(3)	[73]	Si(Li) with fixed activity

Table XVIII summarizes various measurements of the branching ratio to the excited state. The branching ratios are claimed to be known to a precision  $\sim 0.1\%$ , and vary within themselves by 4%. This is much smaller than the observed gallium anomaly and is not enough to explain our results.

- 
- [1] B. Pontecorvo, Neutrino experiments and the problem of conservation of leptonic charge, *Sov. Phys. JETP* **26**, 165 (1968).
- [2] S. Gariazzo, C. Giunti, M. Laveder, Y. F. Li, and E. M. Zanarin, Light sterile neutrinos, *Journal of Physics G: Nuclear and Particle Physics* **43**, 033001 (2015).
- [3] C. Giunti and T. Lasserre,  $\nu$ -scale sterile neutrinos, *Annual Review of Nuclear and Particle Science* **69**, 163 (2019), <https://doi.org/10.1146/annurev-nucl-101918-023755>.
- [4] S. Böser, C. Buck, C. Giunti, J. Lesgourgues, L. Ludhova, S. Mertens, A. Schukraft, and M. Wurm, Status of light sterile neutrino searches, *Progress in Particle and Nuclear Physics* **111**, 103736 (2020).
- [5] A. Diaz, C. Argüelles, G. Collin, J. Conrad, and M. Shaevitz, Where are we with light sterile neutrinos?, *Physics Reports* **884**, 1 (2020).
- [6] S.-H. Seo, Review of sterile neutrino experiments, in *PARTICLE PHYSICS at the Year of 150th Anniversary of the Mendeleev's Periodic Table of Chemical Elements: Proceedings of the Nineteenth Lomonosov Conference on Elementary Particle Physics* (World Scientific, 2021) pp. 10–16.
- [7] B. Dasgupta and J. Kopp, Sterile neutrinos, arXiv preprint arXiv:2106.05913 (2021).
- [8] P. Janot and S. Jadach, Improved Bhabha cross section at LEP and the number of light neutrino species (2020), arXiv:1912.02067 [hep-ph].
- [9] J. Abdallah *et al.* (DELPHI), Photon events with missing energy in  $e^+ - e^-$  collisions at  $s^{1/2} = 130$  GeV to 209 GeV, *Eur. Phys. J. C* **38**, 395 (2005), arXiv:hep-ex/0406019.
- [10] P. Achard *et al.* (L3), Single photon and multiphoton events with missing energy in  $e^+e^-$  collisions at LEP, *Phys. Lett. B* **587**, 16 (2004), arXiv:hep-ex/0402002.
- [11] Precision electroweak measurements on the Z resonance, *Physics Reports* **427**, 257 (2006).
- [12] N. Aghanim *et al.* (Planck), Planck 2018 results. VI. Cosmological parameters, *Astron. Astrophys.* **641**, A6 (2020), arXiv:1807.06209 [astro-ph.CO].
- [13] B. D. Fields, K. A. Olive, T.-H. Yeh, and C. Young, Big-Bang Nucleosynthesis after Planck, *JCAP* **03**, 010, [Erratum: JCAP 11, E02 (2020)], arXiv:1912.01132 [astro-ph.CO].
- [14] M. M. Ivanov, M. Simonović, and M. Zaldarriaga, Cosmological Parameters and Neutrino Masses from the Final Planck and Full-Shape BOSS Data, *Phys. Rev. D* **101**, 083504 (2020), arXiv:1912.08208 [astro-ph.CO].
- [15] S. L. Glashow, The future of elementary particle physics, in *Quarks and Leptons*, edited by M. Lévy, J.-L. Basdevant, D. Speiser, J. Weyers, R. Gastmans, and M. Jacob (Springer US, Boston, MA, 1980) pp. 687–713.
- [16] J. Schechter and J. W. F. Valle, Neutrino masses in  $su(2) \otimes u(1)$  theories, *Phys. Rev. D* **22**, 2227 (1980).
- [17] R. N. Mohapatra and G. Senjanović, Neutrino mass and spontaneous parity nonconservation, *Phys. Rev. Lett.* **44**, 912 (1980).
- [18] P. Minkowski,  $\mu \rightarrow e\gamma$  at a rate of one out of  $10^9$  muon decays?, *Physics Letters B* **67**, 421 (1977).
- [19] C. Athanassopoulos, L. B. Auerbach, R. L. Burman, I. Cohen, D. O. Caldwell, B. D. Dieterle, J. B. Donahue, A. M. Eisner, A. Fazely, F. J. Federspiel, *et al.* (LSND Collaboration), Evidence for  $\bar{\nu}_\mu \rightarrow \bar{\nu}_e$  oscillations from the lsnd experiment at the los alamos meson physics facility, *Phys. Rev. Lett.* **77**, 3082 (1996).
- [20] A. Aguilar, L. B. Auerbach, R. L. Burman, D. O. Caldwell, E. D. Church, A. K. Cochran, J. B. Donahue, A. Fazely, G. T. Garvey, R. M. Gunasingha, *et al.* (LSND Collaboration), Evidence for neutrino oscillations from the observation of  $\bar{\nu}_e$  appearance in a  $\bar{\nu}_\mu$  beam, *Phys. Rev. D* **64**, 112007 (2001).
- [21] T. A. Mueller, D. Lhuillier, M. Fallot, A. Letourneau, S. Cormon, M. Fechner, L. Giot, T. Lasserre, J. Martino, G. Mention, A. Porta, and F. Yermia, Improved predictions of reactor antineutrino spectra, *Phys. Rev. C* **83**, 054615 (2011).
- [22] G. Mention, M. Fechner, T. Lasserre, T. A. Mueller, D. Lhuillier, M. Cribier, and A. Letourneau, Reactor antineutrino anomaly, *Phys. Rev. D* **83**, 073006 (2011).
- [23] P. Adamson, F. P. An, I. Anghel, A. Aurisano, A. B. Balantekin, H. R. Band, G. Barr, M. Bishai, A. Blake, S. Blyth, *et al.* (Daya Bay Collaboration and MINOS Collaboration), Limits on active to sterile neutrino oscillations from disappearance searches in the MINOS, Daya Bay, and Bugey-3 experiments, *Phys. Rev. Lett.* **117**, 151801 (2016).

- [24] J. N. Abdurashitov, V. N. Gavrin, S. V. Girin, V. V. Gorbachev, T. V. Ibragimova, A. V. Kalikhov, N. G. Khairnasov, T. V. Knodel, V. N. Kornoukhov, I. N. Mirmov, *et al.* (The SAGE Collaboration), Measurement of the response of a gallium metal solar neutrino experiment to neutrinos from a  $^{51}\text{Cr}$  source, *Phys. Rev. C* **59**, 2246 (1999).
- [25] J. N. Abdurashitov, V. N. Gavrin, S. V. Girin, V. V. Gorbachev, P. P. Gurkina, T. V. Ibragimova, A. V. Kalikhov, N. G. Khairnasov, T. V. Knodel, V. A. Matveev, *et al.*, Measurement of the response of a ga solar neutrino experiment to neutrinos from a  $^{37}\text{Ar}$  source, *Phys. Rev. C* **73**, 045805 (2006).
- [26] W. Hampel, G. Heusser, J. Kiko, T. Kirsten, M. Laubenstein, E. Pernicka, W. Rau, U. Rönn, C. Schlosser, M. Wójcik, *et al.*, Final results of the  $^{51}\text{Cr}$  neutrino source experiments in GALLEX, *Physics Letters B* **420**, 114 (1998).
- [27] F. Kaether, W. Hampel, G. Heusser, J. Kiko, and T. Kirsten, Reanalysis of the GALLEX solar neutrino flux and source experiments, *Physics Letters B* **685**, 47 (2010).
- [28] P. Abratenko, R. An, J. Anthony, L. Arellano, J. Asaadi, A. Ashkenazi, S. Balasubramanian, B. Baller, C. Barnes, G. Barr, *et al.*, Search for an excess of electron neutrino interactions in MicroBooNE using multiple final state topologies, arXiv preprint arXiv:2110.14054 (2021).
- [29] P. B. Denton, Sterile neutrino searches with MicroBooNE: Electron neutrino disappearance (2021), arXiv:2111.05793 [hep-ph].
- [30] C. A. Argüelles, I. Esteban, M. Hostert, K. J. Kelly, J. Kopp, P. A. N. Machado, I. Martinez-Soler, and Y. F. Perez-Gonzalez, MicroBooNE and the  $\nu_e$  interpretation of the MiniBooNE low-energy excess (2021), arXiv:2111.10359 [hep-ph].
- [31] M. A. Acero, C. Giunti, and M. Laveder, Limits on  $\nu_e$  and  $\bar{\nu}_e$  disappearance from gallium and reactor experiments, *Phys. Rev. D* **78**, 073009 (2008).
- [32] J. N. Abdurashitov, V. N. Gavrin, S. V. Girin, V. V. Gorbachev, T. V. Ibragimova, A. V. Kalikhov, N. G. Khairnasov, T. V. Knodel, I. N. Mirmov, A. A. Shikhin, *et al.* (SAGE Collaboration), Measurement of the solar neutrino capture rate with gallium metal, *Phys. Rev. C* **60**, 055801 (1999).
- [33] J. Kozlova, E. Veretenkin, V. Gavrin, A. Zvir, T. Ibragimova, and V. Tarasov, Measurement of activity of an artificial neutrino source in the BEST experiment by the calorimetric method, *Physics of Atomic Nuclei* **83**, 958 (2020).
- [34] V. Gavrin, T. Ibragimova, J. Kozlova, V. Tarasov, E. Veretenkin, and A. Zvir, Measurement of neutrino source activity in the experiment BEST by calorimetric method, *Journal of Instrumentation* **16** (04), P04012.
- [35] C. Zhou, *Nucl. Data Sheets* **63**, 229 (1991).
- [36] J. N. Bahcall, B. T. Cleveland, R. Davis, I. Dostrovsky, J. C. Evans, W. Frati, G. Friedlander, K. Lande, J. K. Rowley, R. W. Stoenner, and J. Weneser, Proposed solar-neutrino experiment using  $^{71}\text{Ga}$ , *Phys. Rev. Lett.* **40**, 1351 (1978).
- [37] I. R. Barabanov, E. P. Veretenkin, V. N. Gavrin, S. N. Danshin, L. A. Eroshkina, G. T. Zatsepin, Y. I. Zakharov, S. A. Klimova, Y. B. Klimov, T. V. Knodel, A. V. Kopylov, I. V. Orekhov, A. A. Tikhonov, and M. I. Churmaeva, Pilot installation of the gallium-germanium solar neutrino telescope, *AIP Conference Proceedings* **126**, 175 (1985), <https://aip.scitation.org/doi/pdf/10.1063/1.35146>.
- [38] B. Cleveland, V. Gavrin, V. Gorbachev, T. Ibragimova, T. Knodel, Y. Malyskhin, I. Mirmov, and E. Veretenkin, Use of enriched isotopes to measure efficiency of chemical extraction in the SAGE solar neutrino experiment, *International Journal of Mass Spectrometry* **392**, 41 (2015).
- [39] W. Hampel and L. P. Remsberg, Half-life of  $^{71}\text{Ge}$ , *Phys. Rev. C* **31**, 666 (1985).
- [40] S. Danshin, A. Kopylov, and V. Yants, Small gas proportional counters filled with an Ar-CO<sub>2</sub> mixture for counting of ultra-low activities of  $^{37}\text{Ar}$ , *Nuclear Instruments and Methods in Physics Research Section A: Accelerators, Spectrometers, Detectors and Associated Equipment* **349**, 466 (1994).
- [41] J. N. Abdurashitov, V. N. Gavrin, V. V. Gorbachev, P. P. Gurkina, T. V. Ibragimova, A. V. Kalikhov, N. G. Khairnasov, T. V. Knodel, I. N. Mirmov, A. A. Shikhin, *et al.* (SAGE Collaboration), Measurement of the solar neutrino capture rate with gallium metal. III. results for the 2002–2007 data-taking period, *Phys. Rev. C* **80**, 015807 (2009).
- [42] S. R. Elliott, An analytical expression for the extended pulse shape in a proportional counter, *Nucl. Instr. and Meth. A* **290**, 158 (1990), erratum *Nucl. Instr. and Meth. A* **297**, 536 (1990).
- [43] V. Gavrin and V. Gorbachev, Background of external  $\gamma$  radiation in the proportional counters of the SAGE experiment, *Physics of Atomic Nuclei* **66**, 268 (2003).
- [44] V. Gavrin, V. Gorbachev, and I. Mirmov, Effect of radon on SAGE results, *Physics of Atomic Nuclei* **65**, 843 (2002).
- [45] J. N. Bahcall, Gallium solar neutrino experiments: Absorption cross sections, neutrino spectra, and predicted event rates, *Phys. Rev. C* **56**, 3391 (1997).
- [46] H. Ejiri, H. Akimune, Y. Arimoto, I. Daito, H. Fujimura, Y. Fujita, M. Fujiwara, K. Fushimi, M. Greenfield, M. Harakeh, *et al.*, Spin-isospin responses of  $^{71}\text{Ga}$  for solar neutrinos studied by  $^{71}\text{Ga} (^3\text{He}, t\gamma) ^{71}\text{Ge}$  reaction, *Physics Letters B* **433**, 257 (1998).
- [47] D. Frekers, H. Ejiri, H. Akimune, T. Adachi, B. Bilgier, B. Brown, B. Cleveland, H. Fujita, Y. Fujita, M. Fujiwara, *et al.*, The  $^{71}\text{Ga}(^3\text{He},t)$  reaction and the low-energy neutrino response, *Physics Letters B* **706**, 134 (2011).
- [48] D. Frekers, M. Simon, C. Andreoiu, J. Bale, M. Brodeur, T. Brunner, A. Chaudhuri, U. Chowdhury, J. Crespo López-Urrutia, P. Delheij, *et al.*, Penning-trap Q-value determination of the  $\text{Ga}71(\nu, e^-)\text{Ge}71$  reaction using threshold charge breeding of on-line produced isotopes, *Physics Letters B* **722**, 233 (2013).
- [49] D. Frekers, T. Adachi, H. Akimune, M. Alanssari, B. A. Brown, B. T. Cleveland, H. Ejiri, H. Fujita, Y. Fujita, M. Fujiwara, *et al.*, Precision evaluation of the  $^{71}\text{Ga}(\nu_e, e^-)$  solar neutrino capture rate from the  $(^3\text{He}, t)$  charge-exchange reaction, *Phys. Rev. C* **91**, 034608 (2015).
- [50] W. Haxton, Cross section uncertainties in the gallium neutrino source experiments, *Physics Letters B* **431**, 110 (1998).
- [51] V. Barinov, B. Cleveland, V. Gavrin, D. Gorbunov, and T. Ibragimova, Revised neutrino-gallium cross section and prospects of best in resolving the gallium anomaly, *Phys. Rev. D* **97**, 073001 (2018).
- [52] J. Kostensalo, J. Suhonen, C. Giunti, and P. Srivastava,

- The gallium anomaly revisited, *Physics Letters B* **795**, 542 (2019).
- [53] S. Semenov, Cross section of neutrino absorption by the gallium-71 nucleus, *Physics of Atomic Nuclei* **83**, 1549 (2020).
- [54] K. Abusaleem and B. Singh, Nuclear data sheets for  $A = 71$ , *Nuclear Data Sheets* **112**, 133 (2011).
- [55] M. Alanssari, D. Frekers, T. Eronen, L. Canete, J. Hakala, M. Holl, A. Jokinen, A. Kankainen, J. Koponen, I. Moore, D. Nesterenko, I. Pohjalainen, J. Reinikainen, S. Rinta-Antila, and A. Voss, Precision Ga71–Ge71 mass-difference measurement, *International Journal of Mass Spectrometry* **406**, 1 (2016).
- [56] L. Machlan, J. Gramlich, L. Powell, and G. Lambert, Absolute isotopic abundance ratio and atomic weight of a reference sample of gallium, *Journal of Research of the National Bureau of Standards* **91**, 323 (1986).
- [57] G. L. Fogli, E. Lisi, A. Marrone, D. Montanino, and A. Palazzo, Getting the most from the statistical analysis of solar neutrino oscillations, *Phys. Rev. D* **66**, 053010 (2002).
- [58] K. Olive, Review of particle physics, *Chinese Physics C* **38**, 090001 (2014).
- [59] P. Coloma, P. Huber, and T. Schwetz, Statistical interpretation of sterile neutrino oscillation searches at reactors, *The European Physical Journal C* **81**, 1 (2021).
- [60] J. M. Berryman, P. Coloma, P. Huber, T. Schwetz, and A. Zhou, Statistical significance of the sterile-neutrino hypothesis in the context of reactor and gallium data (2021), [arXiv:2111.12530 \[hep-ph\]](https://arxiv.org/abs/2111.12530).
- [61] M. Andriamirado, A. B. Balantekin, H. R. Band, C. D. Bass, D. E. Bergeron, D. Berish, N. S. Bowden, J. P. Brodsky, C. D. Bryan, T. Classen, *et al.* (PROSPECT Collaboration), Improved short-baseline neutrino oscillation search and energy spectrum measurement with the PROSPECT experiment at HFIR, *Phys. Rev. D* **103**, 032001 (2021).
- [62] N. a. Skrobova, New results from the DANSS experiment, *International Journal of Modern Physics A* **35**, 2044015 (2020), <https://doi.org/10.1142/S0217751X20440157>.
- [63] H. Almazán, L. Bernard, A. Blanchet, A. Bonhomme, C. Buck, P. del Amo Sanchez, I. El Atmani, J. Haser, F. Kandzia, S. Kox, *et al.* (STEREO Collaboration), Improved sterile neutrino constraints from the STEREO experiment with 179 days of reactor-on data, *Phys. Rev. D* **102**, 052002 (2020).
- [64] M. Aker, K. Altenmüller, A. Beglarian, J. Behrens, A. Berlev, U. Besserer, B. Bieringer, K. Blaum, F. Block, B. Bornschein, *et al.* (KATRIN Collaboration), Bound on  $3 + 1$  active-sterile neutrino mixing from the first four-week science run of KATRIN, *Phys. Rev. Lett.* **126**, 091803 (2021).
- [65] Z. Atif, J. Choi, H. Jang, J. Jang, S. Jeon, K. Joo, K. Ju, D. Jung, J. Kim, J. Kim, *et al.*, Search for sterile neutrino oscillation using RENO and NEOS data, [arXiv preprint arXiv:2011.00896](https://arxiv.org/abs/2011.00896) (2020).
- [66] C. Giunti, Y. Li, C. Ternes, and Y. Zhang, Neutrino-4 anomaly: Oscillations or fluctuations?, *Physics Letters B* **816**, 136214 (2021).
- [67] A. Serebrov and R. Samoilov, Analysis of the results of the Neutrino-4 experiment on the search for the sterile neutrino and comparison with results of other experiments, *JETP Letters* **112**, 199 (2020).
- [68] W. Hampel, J. Handt, G. Heusser, D. Kaether, J. Kiko, T. Kirsten, M. Laubenstein, E. Neder, E. Pernicka, W. Rau, *et al.*, Verification tests of the GALLEX solar neutrino detector, with  $^{71}\text{Ge}$  produced in-situ from the beta-decay of  $^{71}\text{As}$ , *Physics Letters B* **436**, 158 (1998).
- [69] M. Agostini, K. Altenmüller, S. Appel, D. Jeschke, B. Neumair, L. Oberauer, L. Papp, S. Schönert, F. von Feilitzsch, V. Atroshchenko, *et al.*, Comprehensive measurement of pp-chain solar neutrinos, *Nature* **562**, 505 (2018).
- [70] S. Fisher and R. Hershberger, Branching ratios for ec decay of  $^7\text{Be}$  and  $^{51}\text{Cr}$ , *Nuclear Physics A* **423**, 121 (1984).
- [71] A. Konstantinov, T. Sazonova, S. Sepman, A. Zanevsky, and N. Karmalitsyn, Determination of x-ray and gamma-ray emission probabilities of  $^{51}\text{Cr}$  and  $^{88}\text{Y}$ , *Nuclear Instruments and Methods in Physics Research Section A: Accelerators, Spectrometers, Detectors and Associated Equipment* **339**, 200 (1994).
- [72] P. Yalçın and Y. Kurucu, Emission probabilities of k x- and  $\gamma$ -rays following  $^{51}\text{Cr}$  and  $^{67}\text{Ga}$  decay, *Applied Radiation and Isotopes* **62**, 63 (2005).
- [73] D. S. Moreira, M. F. Koskinas, I. M. Yamazaki, and M. S. Dias, Determination of  $^{51}\text{Cr}$  and  $^{241}\text{Am}$  x-ray and gamma-ray emission probabilities per decay, *Applied Radiation and Isotopes* **68**, 596 (2010), the 7th International Topical Meeting on Industrial Radiation and Radio isotope Measurement Application(IRRMA-7).